博士論文

Superconducting transport phenomena in ballistic nanowire Josephson junctions

(弾道的ナノ細線ジョセフソン接合における
超伝導輸送現象)

上田　健人

Contents

6   Half-integer Shapiro steps in a short ballistic InAs nanowire Josephson junction   86

7 Summary and Outlook

Abstract

A Majorana fermion is a superposition of an electron and a hole, and is expected to find application in topological quantum calculations. Our work has aimed to realize Majorana fermions in the absence of a magnetic field using the hybrid junction of an s-wave superconductor and two parallel semiconductor nanowires. A key requirement for the realization of Majorana fermions is the occurrence of Cooper pair splitting in the one-dimensional channels formed in the two nanowires; however, this has never been observed.

First, we used an InAs double nanowire to fabricate a ballistic and gate-tunable double-nanowire Josephson junction. We distinguished the gate-tunable operation of each single nanowire and a double nanowire from observation of quantized conductance. We measured the supercurrent flowing through the single nanowires and the double nanowire separately, and for the first time in the world, demonstrated Cooper pair splitting in the one-dimensional channels [1]. In addition, we achieved gate-tuning of the Cooper pair splitting energy and succeeded in increasing the inter-wire pairing strength sufficiently to create the necessary conditions for realizing Majorana bound states without the presence of a magnetic field.

One of the ways to employ the Josephson junction device for detecting Majorana bound states is to observe the vanishing of the odd-numbered Shapiro steps, which reflects the change in the period of the Andreev Bound state of the junction. However, experiments to observe the Shapiro steps in ballistic Josephson junctions of the semiconductor nanowires used in our study have not yet been reported. Thus, we fabricated a ballistic Josephson junction using a single InAs nanowire to measure the Shapiro steps. We succeeded in observing a half-integer Shapiro step as would be theoretically expected [2]. This paves the way to use

the measurement of the Shapiro step as a useful tool for detecting the presence of Majorana fermions in a double-nanowire Josephson junction.

Chapter 1

Introduction and motivation

I. Introduction and motivation

In recent years, considerable effort has been devoted to the development of quantum computers. A major challenge associated with this development is the correction of errors that occur during the process of quantum operations at the device level. In a topological quantum computer using Majorana fermions (MFs), typical topological particles, such as qubits, can overcome this challenge because braiding Majorana modes form the basis of topologically protected quantum gates which would be tolerant of local perturbations. In this context, there has been growing interest in searching for MFs in solid-state devices, particularly triggered by the report from TuDelft in 2012 that MFs have been observed in hybrid s-wave superconductor (SC)-semiconductor nanowire (NW) devices [3]. Indeed quite a few experiments to feature MFs have been performed, such as the tunneling conductance measurement of SC-NW devices [4, 5], scanning tunneling microscopy of ferromagnetic atomic chains on an SC [6], vortex cores in topological SCs [7], and measurement of the Shapiro-step of topological insulator Josephson junctions [8, 9]. As a result of these experiments, NW-based devices appear to be the most promising platform for realizing topological quantum computing based on braiding operations. This is because Majorana bound states (MBSs) are formed at the edge of the SC in contact with the NW, thereby allowing for simple ways of local braiding [10, 11].

MBSs in hybrid SC-NW devices only appear in the presence of a strong mag-

netic field. However, this causes an essential problem in generating robust Majorana states, because the proximity-induced SC gap in the NW is only well established for zero or sufficiently weak magnetic fields to avoid the generation of any finite subgap conductance or quasi-particle excitation. Note the quasi-particle excitation can degrade the topological protection (known as "quasi-particle poisoning"). However, it has been proposed that MBSs can be generated in the absence of a magnetic field using two time-reversal symmetric one-dimensional (1D) channel NWs coupled to an s-wave SC. The topological transition in this system can be induced by ensuring that the inter-wire pairing is larger than the intra-wire pairing instead of applying a strong magnetic field. Here, inter-wire pairing indicates that the tunneling of Cooper paired electrons are split between the two NWs (known as Cooper pair splitting, CPS) whereas intra-wire pairing entails local Cooper pair tunneling to one of the respective NWs (known as local pair tunneling, LPT). The concept of CPS was experimentally demonstrated for two semiconductor quantum dots in 2009, and, although this gave rise to subsequent studies of the underlying physics, these studies were restricted to quantum dots rather than 1D channel NWs, probably owing to the technical difficulty of device fabrication. These circumstances motivated us to focus on this topic of double NW (DNW) Josephson devices to study the feasibility of generating CPS across two NWs with 1D channels and thereby MBSs, in the absence of a magnetic field.

II.   Outline of this thesis

In this work we fabricated samples of a ballistic Josephson junction with a gate-tunable InAs parallel DNW coupled to two aluminum SCs. This approach

is necessary for two reasons. First, it would allow the inter- and intra-pairing strength for the two NWs to be evaluated from measurements of the supercurrent resulting from CPS and LTP, respectively. The theory predicts that the CPS efficiency depends on the 1D electron-electron interaction [12], such that it is useful to electrically modulate the number of 1D propagating modes in the respective NWs. Second, the observation of 1D quantized conductance steps in the ballistic transport of NWs facilitates evaluation of the number of 1D channels and also helps to increase the supercurrent flow through the Josephson junction. Finally, we can use the same device that was fabricated for CPS measurement for Shapiro-step measurement to signify the presence of MBSs. Therefore, we made our best effort to improve the conventional fabrication technique to raise the quality of the interface between the NWs and Al SCs and shorten the distance between the Al SCs. In addition, we endeavored to develop a technique to form separate top gates for the junction to enable the carrier density in each NW to be independently controlled.

We first used the fabricated device and measured the transport properties under the normal state conditions, and confirmed ballistic conduction of the NWs and the gate tunability of the propagating 1D channels. This enabled us to classify the gate voltage regions to determine whether only one of the NWs is conductive or whether both NWs are conductive. Then we turned on the superconducting conditions to characterize the supercurrent resulting from CPS for the DNW and LPT for the respective single NWs with the two gate voltages as parameters. We succeeded in clearly distinguishing the contributions to the supercurrent as a result of CPS and LPT, and revealed the increasing CPS efficiency by decreasing the number of propagating 1D modes or increasing the electron-electron interaction. Finally, this result allowed us to confirm that the necessary conditions for intra-

10

and inter-wire pairing to generate the MBSs in the absence of a magnetic field are satisfied with our device configuration. (**K. Ueda**, S. Matsuo, H. Kamata, S. Baba, Y. Sato, Y. Takeshige, K. Li, S. Jeppesen, L. Samuelson, H. Xu, S. Tarucha, Science Advances 5, eaaw2194).

On realizing that the fabricated DNW Josephson junctions could be valuable devices for hosting zero-magnetic field MBSs, we proceeded to the next stage to detect the MBSs using the same device. Although several approaches have been demonstrated to experimentally trace MFs, including the observation of a zero-bias anomaly in the tunneling conductance, the absence of odd-numbered Shapiro steps, and half-quantization of the thermal conductance, it is still debatable which one of these approaches is the most reliable. In reality, the zero-bias anomaly is often studied in the experiments of NWs but it is frequently argued that it can be mimicked by the formation of Andreev bound states or disordered states. Thus, we decided not to become involved in this argument and concentrate on the experiment based on the Shapiro step.

In a topological SC with MFs formed at the edge, the Andreev bound state in the Josephson phase is 4π periodic instead of 2π. This can be probed by exploiting the AC Josephson effect. When the Josephson junction is exposed to microwave radiation, the Shapiro steps are identified in the form of voltage plateaus at integer multiples of the quantized value (h/2e $\times$ frequency) against the current sweep. The transition to topological SC results in the disappearance of the odd-numbered Shapiro steps. Although this is a convenient technique with which to explore the Majorana physics, we first needed to understand the physics of the AC Josephson effect in ballistic NW Josephson junctions. Apart from this, we had to develop an experimental technique whereby the weak Josephson current through the NW could be detected. In particular, the AC Josephson effect of ballistic

11

junctions, where the junction is shorter than the coherence length of the superconductor and the mean free path of the NW, is theoretically predicted to produce fractional Shapiro steps, however this has not been studied experimentally. Therefore, we started by setting up the experimental equipment for the Shapiro-step measurement and by characterizing the features of the ballistic Josephson junctions using a single InAs NW. We clearly observed half-integer Shapiro steps and their dependence on the top gate voltage and temperature. On the basis of these results, we were able to clarify the relation between the half-integer Shapiro steps and the current phase relation of the short ballistic Josephson junction. This expertise ultimately paved the way for the observation of Majorana fermions in the ballistic DNW Josephson junction in the absence of a magnetic field. (**K. Ueda**, S. Matsuo, H. Kamata, Y. Sato, Y. Takeshige, K. Li, L. Samuelson, H. Q. Xu, S. Tarucha, Phys. Rev. Research 2, 033435)

Chapter 2

Background

This study focuses on the flow of supercurrent through Josephson junctions, Cooper pair splitting, and the AC Josephson effect. In this chapter, we explain the fundamental concepts behind these phenomena.

I. Andreev Reflection

A. Andreev reflection

Andreev reflection (AR) occurs at the interface between a normal metal conductor and an SC [13]. Fig. 1 shows a schematic illustration of AR when one electron is incident on the normal metal-SC interface from the normal metal at energies less than the superconducting energy gap and one hole of opposite spin and velocity to the incident electron is reflected. In the SC, a pair of electrons with upward and downward spins is formed such that the incident electron forms a Cooper pair with another electron at the interface. In this process, an electron is taken from the normal metal, resulting in a single hole being retroreflected to the normal metal. Note that AR preserves the phase coherence; therefore, the phase difference between the paired electron and hole is given by $\pi/2$ plus the phase of the superconducting order parameter.

13
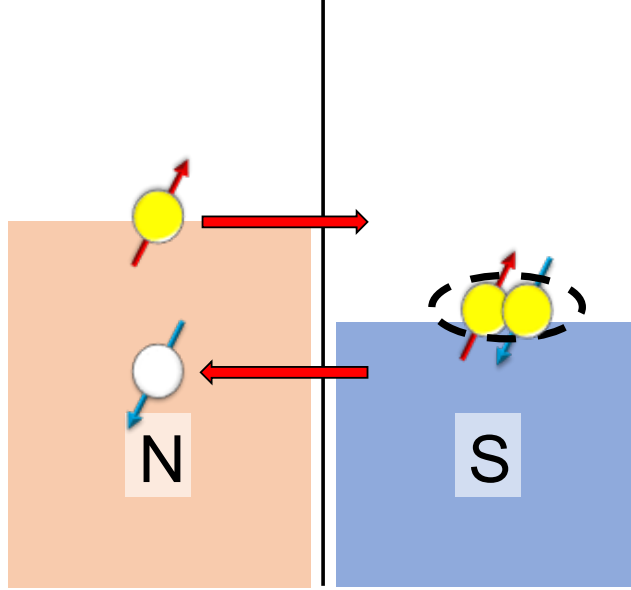
FIG. 1. Schematic of movement of an electron and hole in the AR process. An electron (yellow) is reflected as a hole (white) on the interface between a normal metal conductor and an SC.

The AR mechanism is explained using the Bogoliubov de Gennes (BdG) equation.

$$\begin{pmatrix} H(r) & \Delta(r) \\ \Delta(r)^* & -H(r) \end{pmatrix} \begin{pmatrix} u(r) \\ v(r) \end{pmatrix} = E \begin{pmatrix} u(r) \\ v(r) \end{pmatrix}, \tag{1}$$

where $H(r) = (\mathbf{p} - e\mathbf{A})/2m - E_F$, $\Delta(r) = \Delta_0 \exp(i\theta)$. E_F and $\mathbf{A}$ are the Fermi energy and vector potential, respectively. First, we consider the interface from the normal metal. When an electron with a wave number of k is incident on the interface from the normal metal, the wave function of the normal metal is written

as

$$\Psi^N(r) = \left[\begin{pmatrix} 1 \\ 0 \end{pmatrix} e^{ik_+ x} + \begin{pmatrix} 1 \\ 0 \end{pmatrix} e^{-ik_+ x} r^{ee} + \begin{pmatrix} 0 \\ 1 \end{pmatrix} e^{ik_- x} r^{he} \right] \frac{e^{ipy}}{\sqrt{W}}, \quad (2)$$

where W, $|r^{ee}|^2$, $|r^{he}|^2$, k_+, and k_- are the interface width, the probability of normal reflection, the probability of AR, the wave number of the electron, and the wave number of the hole, respectively. Note that the first, second, and third terms are the wave functions of the incident electron, normal reflected electron, and Andreev reflected hole, respectively. We obtain the following formula under the condition of $\mathbf{A} = 0$ and $\Delta = 0$,

$$\hbar k_{\pm} = \sqrt{2m(E_F \pm E)}. \quad (3)$$

Here, E is the energy based on E_F. When perfect AR occurs ($|r^{he}|^2 = 1$), the momentum becomes $\hbar k_{\pm} = \sqrt{2mE_F}$. This means that the momentum of the electron is the same as that of the hole. This satisfies the retroactivity, meaning that the Andreev-reflected holes return along the exact same path as the incident electrons. If the incident electron is on the Fermi surface, the momentum is expressed as $\hbar k_F$ using the Fermi wavenumber k_F. Because the momentum of the entire Cooper pair is zero as a result of the reflection, the momentum of the hole is also $\hbar k_F$ and the momentum is conserved before and after AR. In fact, the difference between the momentum of the electron and the hole can be ignored if $E \ll E_F$ and $E \neq 0$ because

$$\hbar(k_+ - k_-) \approx E\sqrt{\frac{2m}{E_F}} = \frac{2E}{v_F}. \quad (4)$$

In addition, when $\Delta = 0$, the energy of the incident electron and the reflected hole are $E + E_F$ and $-E + E_F$, respectively. The energy is conserved in the AR

15

process because the energy of the entire Cooper pair is $2E_F$. Therefore, both the momentum and energy are conserved in AR.

Next, we discuss the interface from the SC, the wave function of which is given by

$$\Psi^S(r) = \left[\begin{pmatrix} u \\ ve^{-i\phi} \end{pmatrix} e^{iq_+x}t^{ee} + \begin{pmatrix} ve^{i\phi} \\ u \end{pmatrix} e^{-iq_-x}t^{he} \right] \frac{e^{ipy}}{\sqrt{W}}, \quad (5)$$

where $|t^{ee}|^2$, $|t^{he}|^2$, q_+, and q_- are the probability that the incident electron remains in the SC as an electron, the probability that the incident electron becomes a hole in the SC, the wave number of the electron, and the wave number of the hole, respectively. When substituting this into the BdG equation, the momentum is

$$\hbar q_\pm = \sqrt{2m(E_F \pm (E^2 - \Delta^2)^{1/2})}. \quad (6)$$

u and v are

$$u = \sqrt{\frac{1}{2}\left(1 + i\frac{\Delta^2 - E^2}{E}\right)} \quad (7)$$

$$v = \sqrt{\frac{1}{2}\left(1 - i\frac{\Delta^2 - E^2}{E}\right)}. \quad (8)$$

We connect the two wave functions by introducing a potential barrier $V_0\delta(x)$.

$$\Psi^S(0, y) = \Psi^N(0, y) \quad (9)$$

$$\frac{\partial}{\partial x}(\Psi^N - \Psi^S) = \frac{2m}{\hbar^2}V_0\Psi^N. \quad (10)$$

We obtain

$$r^{ee} = \frac{2r_n\Omega}{(2 - |t_n|^2)\sqrt{E^2 - \Delta^2} + |t_n|^2 E}, \quad (11)$$

$$r^{he} = \frac{|t_n|^2\Delta e^{-i\phi}}{(2 - |t_n|^2)\sqrt{E^2 - \Delta^2} + |t_n|^2 E}, \quad (12)$$

$$r^{eh} = \frac{|t_n|^2\Delta e^{i\phi}}{(2 - |t_n|^2)\sqrt{E^2 - \Delta^2} + |t_n|^2 E}, \quad (13)$$

16

where $t_n = \bar{k}/(\bar{k} + iZ)$, $\bar{k} = k_p/k_F$, $Z = mV_0/\hbar^2 k_F$. When the potential $Z = 0$,

$$r^{ee} = 0, \tag{14}$$

$$r^{he} = \exp[-i\arctan(\sqrt{\Delta^2 - E^2}/E)] \cdot e^{-i\phi}, \tag{15}$$

$$r^{eh} = \exp[-i\arctan(\sqrt{\Delta^2 - E^2}/E)] \cdot e^{-i\phi}. \tag{16}$$

In this case, the electron or hole moves with the phase difference in the AR process. The differential conductance is calculated from these coefficients.

$$G_{NS} = \frac{dI}{dV}\bigg|_{eV} = \frac{2e^2}{h}\sum_p (1 - |r^{ee}|^2 + |r^{he}|^2)\bigg|_{eV=E}, \tag{17}$$

which is known as the Blonder-Tinkham-Klapwijk (BTK) model [14]. Fig. 2 shows G_{NS} as a function of the bias voltage at some Z. Especially, G_{NS} doubles owing to AR when $Z = 0$. Ensuring that Z remains close to zero is highly important for observing the physics of the interface between a superconductor and a semiconductor. In fact, high-efficiency CPS is realized with smaller Z values in our CPS experiments. In addition, it is necessary that the Josephson junction to be measured has a skewed CPR for the observation of half-integer retrosteps. This skewness is related to the probability of the occurrence of Andreev reflection, which means that Z must be small.
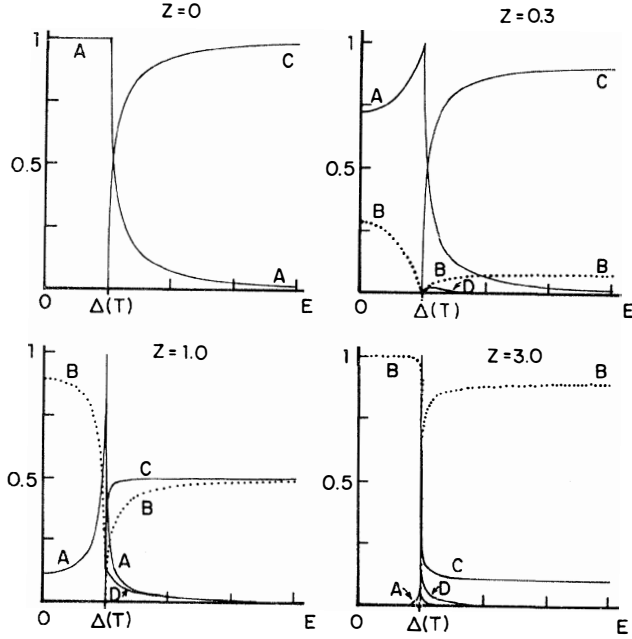
FIG. 2. G_{NS} as a function of the bias voltage at $Z = 0, 0.5, 1.5, 5.0$ [14].

B.   Crossed Andreev reflection

Crossed Andreev reflection (CAR) takes place in two separated normal leads with an SC in between, as shown in Fig. 3, where the distance between the metals is of the order of the SC coherence length. When an electron is incident on the SC from the normal metal, AR or normal reflection occurs. In addition, CAR can occur in the case in which an electron is incident on the SC from one of the normal leads, and the retroreflected hole of opposite spin is not emitted from the same normal lead, but from another lead. In other words, the electron to form a Cooper pair with an incident electron is taken from another lead. Because CAR has the same physical meaning as Cooper pair splitting (CPS), CAR is also referred to as
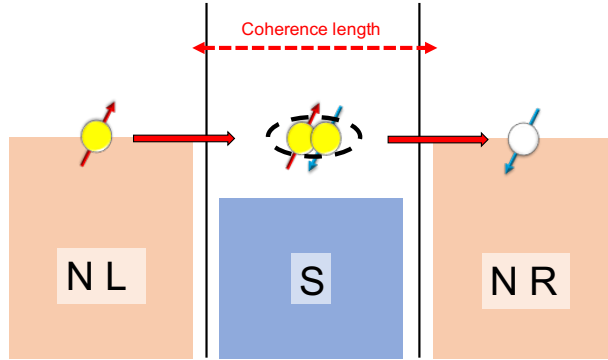
CPS [12, 15–20].

FIG. 3. Schematic of movement of an electron and a hole in the CAR process. An electron (yellow) passes through as a hole (white) when the separation between two normal metals is less than the coherence length of the SC.

C.   Cooper pair splitting

The physics of CPS has been theoretically studied with the use of quantum dots (QDs) [15, 21] (Fig. 4). Our explanation of CPS follows that in Ref [15]. The Coulomb interaction U on D_1 and D_2 and the superconducting gap energy Δ are key components that induce CPS. Basically, Cooper pairs tunneling into the same lead—local pair tunneling (LPT)—must be suppressed by the Coulomb interaction. LPT happens via the two processes, as shown in Fig. 5. The two electrons can tunnel on the same dot and move to the lead at the cost of Coulomb energy U. This virtual state is suppressed by $1/U$. Alternatively, the two electrons move to the same lead in a sequential process, as shown in Fig. 5(b). That is, the two electrons tunnel from the QD to the lead one after another in sequence. The
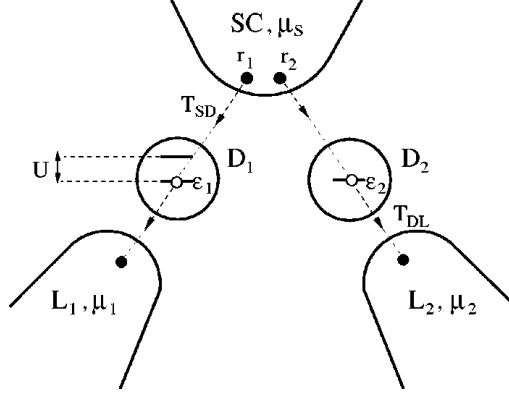
FIG. 4. The setup: Two electrons forming a Cooper pair can tunnel from points $\mathbf{r}_1$ and $\mathbf{r}_2$ of the SC to two dots, D_1 and D_2. The dots are coupled to normal leads L_1 and L_2 [15].

virtual excitation causes $1/\Delta$ in this process. Therefore, the entire LPT process should be suppressed by increasing U and Δ. In addition, it is important to consider the tunnel coupling Γ of QDs. Γ is the sum of Γ_N and Γ_S, which are the tunnel couplings between the QD and the lead and that between the QD and the SC, respectively. In the limit of $\Gamma_N \gg \Gamma_S$, the electron can move from the QDs to the lead faster than it is replaced by new electrons from the SC. Furthermore, the inter-dot coupling Γ_{12} must be smaller than Γ_N to allow the electrons to move to the leads before tunneling between each of the QDs. Under these conditions, CPS happens as a result of LPT suppression.

The CPS and LPT currents are analytically given by using the T-matrix [15, 21]. The CPS component is written as

$$I_{CPS} = \frac{4e\Gamma_S^2}{\Gamma} \left[\frac{\sin(k_F \delta r)}{k_F \delta r} \right]^2 \exp(-\frac{2\delta r}{\pi \xi}), \tag{18}$$

where $\Gamma = \Gamma_1 + \Gamma_2$, Γ_S, k_F, δr, and ξ are the sum of tunnel couplings between
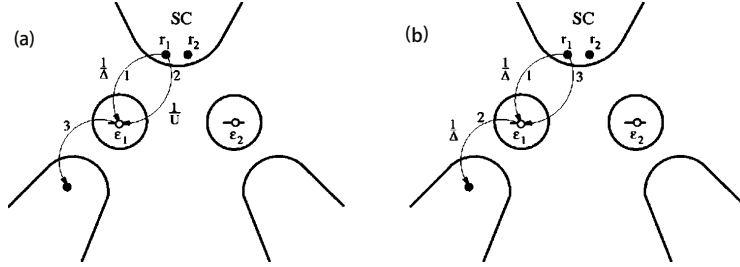
FIG. 5. Schematic of two electrons tunneling via the same dot [15]. (a) Two electron tunnels on the same dot before moving to the lead. (b) After the Cooper pair breaks up, one electron tunnels on the dot while the other dot stays in a quasiparticle state.

the leads and the two quantum dots (1,2), the tunnel coupling between the superconducting lead and two QDs, the Fermi wavelength of the SC, the distance between the SC and the two QDs, and the coherence length of the Cooper pair, respectively. In contrast, the LPT component is expressed as

$$I_{LPT} = \frac{2e\Gamma_S^2\Gamma}{\epsilon}, \quad \frac{1}{\epsilon} = \frac{1}{\pi\Delta} + \frac{1}{U}, \tag{19}$$

where Δ and U are the superconducting energy gap and charging energy of the QDs, respectively. The important point is that the component of the LPT is characterized by U, which is the feature value of the QDs. The ratio of CPS to LPT is given by

$$\frac{I_{CPS}}{I_{LPT}} = \frac{2\epsilon^2}{\Gamma^2} \left[\frac{\sin(k_F \delta r)}{k_F \delta r}\right]^2 \exp(-\frac{2\delta r}{\pi\xi}) \tag{20}$$

The important point in Eq.(20) is that the CPS efficiency, as given by Eq.(20), strongly depends on U, which represents the charging energy or Coulomb interaction of the QDs and Γ. Both the large U and small Γ work to reduce I_{LPT} because the charge is to a greater extent accumulated in the dot to enlarge the interaction effect. On the other hand, the purpose of the small Γ is to increase

21

I_{CPS} because the accumulation effect promotes the CPS process. In reality, the CPS efficiency is enhanced by increasing the values of U and Γ [15].

D. First observation of CPS using QDs

Here, we describe the first observation of CPS using QDs [22], one of many papers concerned with CPS [23–28]. Cooper pairs are entangled pairs of two electrons. The CPS spatially separates two electrons, which consist of a Cooper pair of an SC, into each normal lead. This nonlocality has been successfully tested using paired entangled photons; however, the nonlocality had yet to be realized in the solid state. The first experimental observation of CPS was reported by Hofstetter *et al.*, in 2009 [22] and was demonstrated using QDs. In the system of QDs, the entry of two electrons, which consist of one Cooper pair from an SC, into the same electrode is suppressed because of the Coulomb blockade. Instead, the CPS efficiency is enhanced when each of the two electrons tunnels into different QDs. Fig. 6(a) shows a schematic of the device used in this experiment. In this study, a single InAs NW is utilized as a platform for double QDs, and is connected by aluminum (Al) as an SC and two normal leads through the QDs. Each QD is tuned by varying the top gate voltages, indicated as g1 and g2 in Fig. 6(b). CPS is studied by measuring the differential conductance of each QD and analyzing the correlation between them. The voltage V_{g1} applied to g1 affects QD1. This voltage is kept constant while V_{g2}, which is applied to g2, is changed to tune QD2. The conductance of QD2 indicates Coulomb oscillation. Upon application of a magnetic field that exceeds the critical field of aluminum, the superconductivity of Al vanishes and the metal returns to the normal state, in which CPS is not expected to occur. Indeed, the differential conductance of G_1 of the gray line
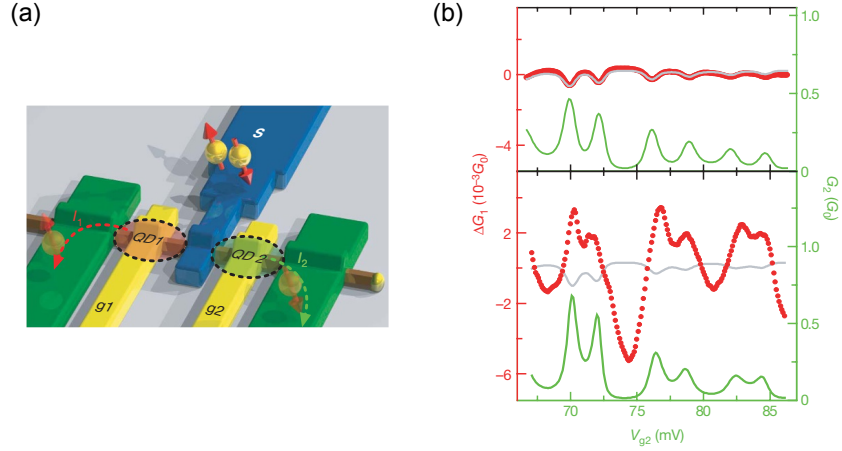
FIG. 6. (a) Schematic of the device with two dots QD1 and QD2 in the single InAs NW used for CPS [22]. (b) Differential conductance of each QD as a function of V_{g2} at $B = 120$ mT (upper panel), and 0 mT (lower panel): the red and gray lines are associated with QD1 and QD2, respectively [22].

that corresponds to the conductance of the SC and the electrode through QD1 is negatively correlated with the differential conductance G_2 of QD2, which has the classical characteristics. On the other hand, G_1, as indicated by the red line, is positively correlated with G_2, which is represented by the green line, indicating the absence of an applied magnetic field. This demonstrates the CPS process, where a Cooper pair is spatially split to enter two electrodes.

E.   Derivation of CPS efficiency using supercurrent

In most previous studies the CPS efficiency was evaluated by measuring the conductance between the SC and normal leads. However, this method could

possibly include quasi-particle components that are not Cooper pairs. Here, we introduce the experiment designed to measure the supercurrent in double-QD Josephson junctions (DQDJJs) [28]. This method can exclude the contribution of quasiparticles and allows the enhanced supercurrent to be detected as a result of CPS, because the Cooper pairs are split to enter each QD separately. Demonstration of CPS by supercurrent measurement means that the coherent transport of the electrons is split to enter different QDs. This implies that the two spins of the split electrons are correlated by way of spin entanglement.

The device is shown in Fig. 7(a), where two self-assembled InAs QDs are connected with the Ti/Al source and drain. Two side gates with voltage V_{sg1} and V_{sg2} are placed near the respective QDs to tune the energy levels of QD1 and QD2, respectively. In addition, a global back gate V_{bg} was used to tune the occupation of the two QDs simultaneously. Note the two tiny QDs are in close proximity to each other, because the CPS process is expected to be efficient when the separation between the two dots is comparable to or shorter than the coherence length of Al.

The CPS process in this device was studied with V_{sg1} and V_{sg2} as parameters to turn on and off the resonance between the SC Fermi energy and the levels of QD1 and QD2. Fig. 7(b) shows the measured superconducting-state stability diagram in the absence of a magnetic field. Line A indicates that QD2 is on resonance, whereas lines B and C indicate that QD2 is off resonance. The CPS process is the most efficient when both QDs are on resonance (see Fig. 7(b) and compare the blue line and the green or red lines in the lower panel).
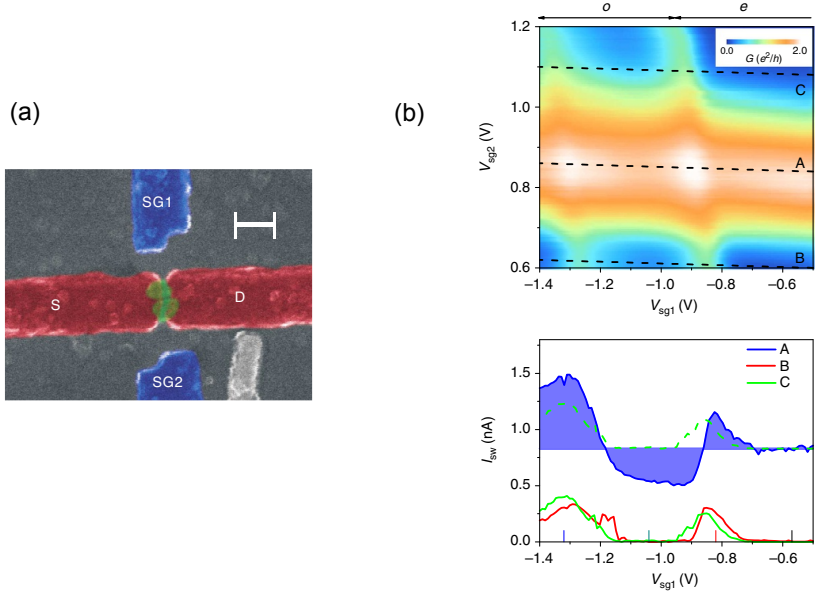
FIG. 7. (a) False color scanning electron microscopy (SEM) image of the double-QD Josephson device. The two gates are used to adjust the energy levels of the two dots independently [28]. (b) Upper panel: the differential conductance in the superconducting state as a function of Vsg1 and Vsg2 with $V_{bg} = 0$ V. Labels o and e represent even and odd electron occupations, respectively. Lower panel: the switching current Isw along lines A, B, and C [28].

25

F.   CPS in two parallel InAs nanowires

The CPS experiments described thus far were performed using two QDs formed on both sides of the SC in a single NW(SNW) (see Fig. 6). In our group, we performed the CPS experiment using two parallel coupled QDs formed in a parallel couple of DNW [27, 29]. Note the two NWs are placed close to each other but are electrically isolated. Fig. 8(a) shows the device structure with such a DNW. Two closely spaced InAs NWs are set in parallel and are coupled with a superconducting lead indicated by S, with two normal metal leads N1 and N2 separately connected with the two NWs; QD1 and QD2 are formed in each NW. Two side gates with voltages V_{sg1} and V_{sg2} are placed near the two NWs to tune the energy levels of each QD. Fig. 8(b) shows an SEM image of the device measured. Note that the two NWs appear to be almost touching each other but are in fact electrically isolated.
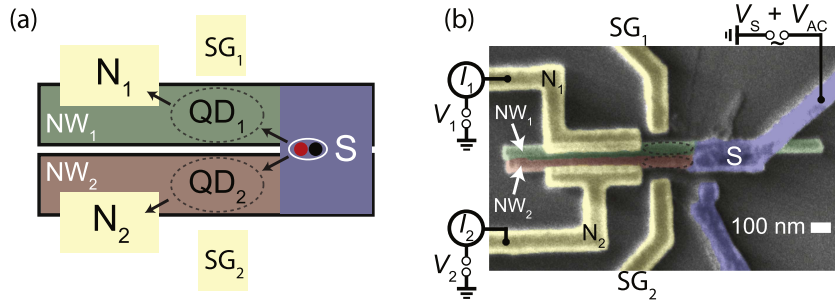

FIG. 8. (a) Schematic of the DNW CPS device [27]. (b) SEM image (false color) of the measured device. The superconductor is in contact with the DNW whereas the normal metal electrode is in contact with each NW [27].
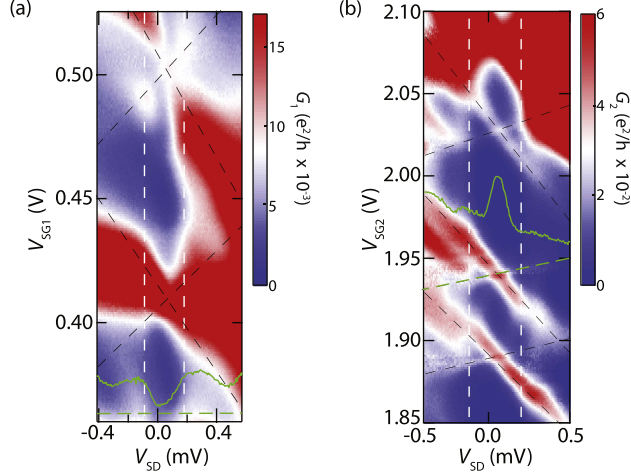
FIG. 9. (a) Differential conductance G_1 of QD$_1$ as a function of both V_{SG1} and V_{SD} shown in Fig. 8. The dashed white lines indicate the energy of the superconducting gap, resulting in the suppressed conductance. The dashed black lines show the formation of the Coulomb blockade [27]. (b) Differential conductance G_2 of QD$_2$ as a function of both V_{SG2} and V_{SD} [27].

Fig. 9(a) and (b) show the conductance characteristics in a zero magnetic field ($B = 0$ T), measured separately for QD1 and QD2, respectively. The Coulomb resonances are observed in each dot by tuning the respective side gate voltage (see intersections of two black dashed lines). The superconducting gap is indicated by the white dashed lines.

Fig. 10(a) and (b) show the differential conductance G_1 and G_2 of QD1 and QD2, respectively, measured in the normal state at $B = 250$ mT. Note that G_1 and G_2 are measured simultaneously as a function of V_{sg1} and V_{sg2}. Several conductance peaks were observed by tuning the respective gate voltages in both the dots. Fig. 10(c) indicates the cuts along the white dashed lines in (a) and (b),

27

and (d) those along the black dashed lines in (a) and (b). The red (green) lines represent G_1 (G_2). In Fig. 10(c), G_2 becomes small at the G_1 peak positions. Similarly, in Fig. 10(d), G_1 becomes small at the G_2 peak positions. This means that a negative correlation exists between G_1 and G_2, and can be well understood using the correlation of a classical electrical circuit model; that is, if the resistance of one QD increases, the current flowing in the other QD increases.

In contrast, Fig. 11 features CPS in the conductance measurement in the superconducting state. The values of G_1 and G_2 in Fig. 11(a) and (b) are measured simultaneously in the same way as in Fig. 10(a) and (b) but at zero-magnetic field. The cuts along the dashed white and black lines in Fig. 11(a) and (b) show the positive correlation in the conductance peaks when both QDs are in resonance. The value of G_1 along the dashed black lines in Fig. 11(d) is observed to be enhanced at the peak positions of G_2. Similarly, the enhancement of G2 along the dashed white lines in Fig. 11(c) is also observed at the peak positions of G_1. This positive correlation is attributed to the effect of CPS.
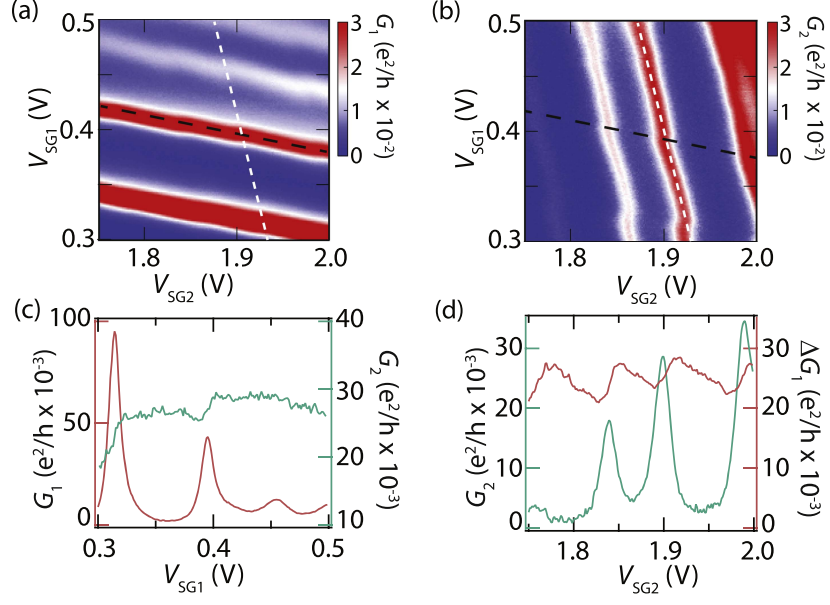
FIG. 10. (a) Differential conductance G_1 of QD$_1$ as a function of both V_{SG1} and V_{SG2} at $B = 250$ mT more than the critical field of aluminum [27]. (b) G_2 for QD$_2$ at more than the critical field [27]. (c) Cross sections along the dashed white lines of (a) and (b) [27]. (d) Cross sections along the dashed black lines of (a) and (b) [27].

FIG. 11. (a) Differential conductance G_1 of QD$_1$ as a function of both V_{SG1} and V_{SG2} [27]. (b) G_2 for QD$_2$ [27]. (c) Cross sections along the dashed white lines of (a) and (b) [27]. (d) Cross sections along the dashed black lines of (a) and (b) [27].
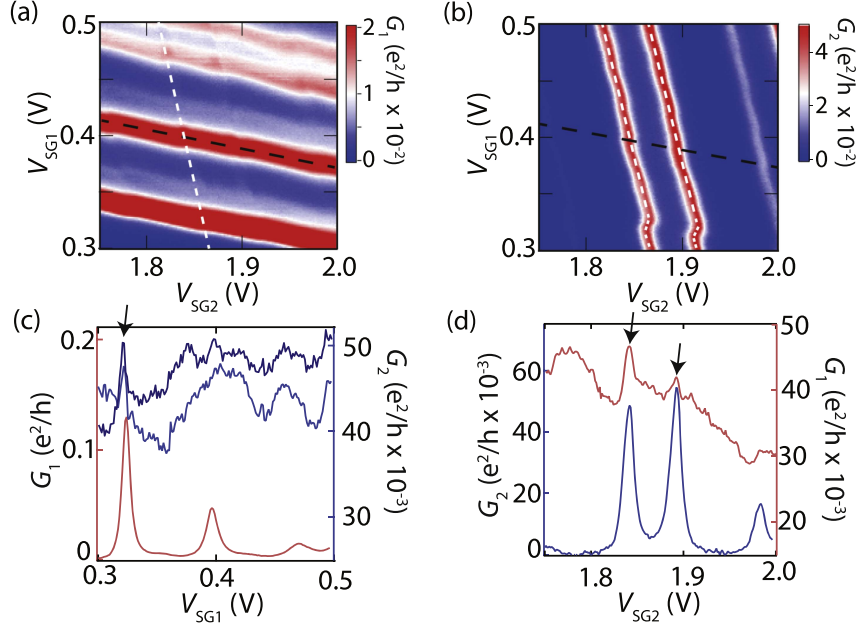
II.   Josephson junction

A.   Multiple Andreev reflections

When an SNS junction is biased with voltage V equivalent to $\pm 2\Delta/e$, carrier tunneling is allowed between the SCs, and the differential conductance of the junction is peaked. This is the so-called quasiparticle tunneling. For the smaller $V < 2\Delta$), no such tunneling occurs but when $V = \pm\Delta/e$, the Fermi energy of the SC on the left and the upper or lower edge of the SC gap on the right

30

is aligned. In this case, a single AR allows quasi-particle tunneling through this junction to generate a differential conductance peak (subgap tunneling). Electrons incoming from the Fermi energy have to form Cooper pairs because they are in the superconducting gap, whereas electrons (holes) at the upper (lower) edge of the gap exit as quasi-particles and do not form Cooper pairs. In addition, when $eV = \pm 2\Delta/n(n = 1, 2, 3\ldots)$, a similar process occurs but via n-1 times ARs. Then, a series of peaks in the differential conductance peaks. This process is known as multiple Andreev reflection (MAR). MAR can be observed when the probability of normal reflection at the SN interface is suppressed owing to the high-quality transparency of the interface. In this sense, ballistic transport in the SNS junction is supported by the observation of MAR.
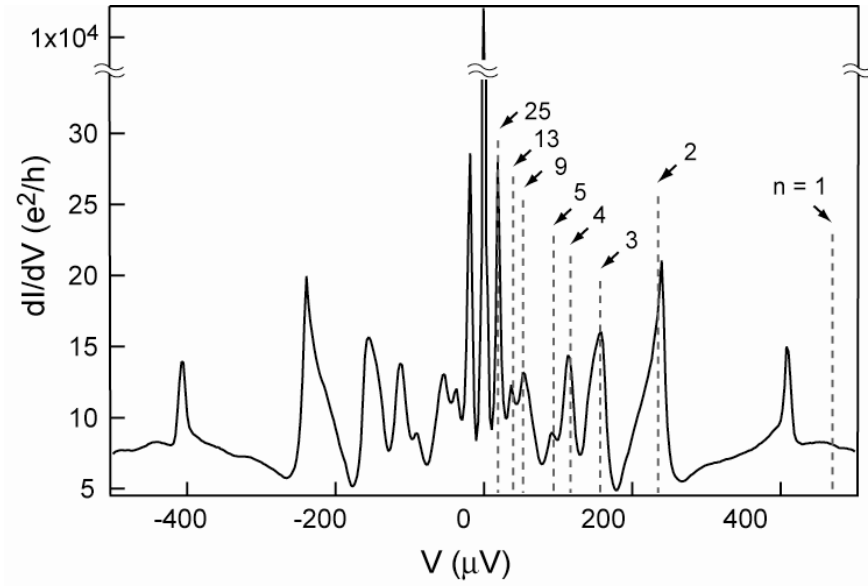

FIG. 12. Typical result of MAR using Ge/Si NWs with Al contacts. [30]

31

B. Andreev bound state

In the SC-NW-SC (SNS) junctions studied here, AR can take place at both SN interfaces. When the ARs are repeated in the junction by preserving the phase coherence, Andreev bound states (ABSs) are formed at discrete energies within the gap (see Fig. 13). We here consider the necessary conditions to establish the ABSs using a couple of assumptions without losing the essence of ABSs. First, the phase of the SC on the left (right) is $\theta/2(-\theta/2)$. Second, N is a normal metal and the electron mean free path therein is shorter than the distance between the two SCs, such that electrons ballistically travel without being scattered in the N region. Lastly, the probability of AR is unity, which means that a single hole reflects perfectly when a single electron is incident on the S region. Under these assumptions, the ABS energy spectrum is obtained by considering the phase that an electron acquires in the AR process. In Fig. 13, we consider the phase exchange between an electron and a hole via the AR process. The electron acquires an additional phase of $-\theta/2 - \varphi$ when it is reflected as AR on the SN interface on the right. Then the hole reflected as a result of AR also acquires the same phase when AR takes place at the interface on the left. We note that $\varphi = \arccos(E/\Delta)$ is the phase that is acquired in the AR process. When an electron or a hole moves in the N region of the junction, it acquires an additional phase proportional to the path length. Consequently, the total phase acquired in the AR process is given by multiples of 2π to maintain the coherence:

$$p_+ L - \theta/2 - \varphi - p_- L - \theta/2 - \varphi = 2n\pi$$
$$p_\pm = \sqrt{2m(E_F \pm E)}/\hbar,$$

(21)

32

where $p_{\pm}$, L, E_F, E, and m are the momentum of the electron or hole; the junction length; the Fermi energy; the eigenenergy of the junction, known as the ABS energy, and the effective mass of the electron, respectively. Given $p_+ - p_- \approx \frac{2E}{v_F}$, $E \ll E_F$, and the ABS energy becomes

$$E_n^+ = \frac{\hbar v_F}{2L}[2(\pi n + \varphi) + \theta]. \tag{22}$$

In addition, considering the inverse process depicted in Fig. 13, we obtain $E_n^- = \frac{\hbar v_F}{2L}[2(\pi n + \varphi) - \theta]$. If the supercurrent flows through the junction, θ does not become zero, in which case the ABS energy is split. In particular, when $L \ll \xi$ of a short ballistic case, the number of bound states is one, and the part on the left, from which $\hbar v_F/2L$ of Eq. (22) is subtracted, becomes:

$$\frac{2EL}{\hbar v_F} = \frac{2E}{\pi \Delta} \frac{L}{\xi} \to 0. \tag{23}$$

Therefore, Eq. (22) results in $-2\varphi = \pm\theta$ in $n = 0$. The ABS energy is given by

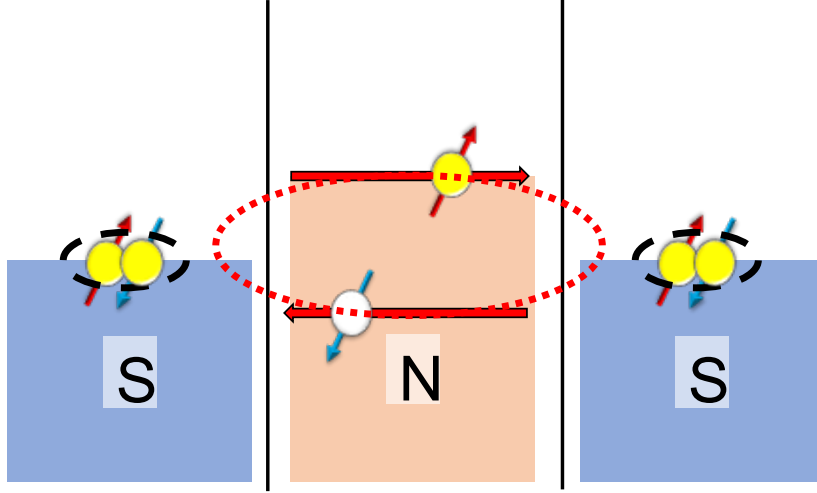$$E = \Delta \cos(\pm\theta/2). \tag{24}$$

FIG. 13. Schematic of ABS process. The discrete energy spectra are formed by AR at both interfaces of S and N.

C. Current phase relation

In a Josephson junction, supercurrent I flows in response to the phase difference ϕ between the two separated SCs. In this case, the so-called current phase relation (CPR) is established between I and ϕ. Generally, the supercurrent is formulated as

$$I = \frac{2e}{\hbar} \frac{dE}{d\theta}, \tag{25}$$

where E is the energy of the ABS. When the junction is short ballistic, E is obtained as

$$E = \Delta[1 - \tau \sin^2(\theta/2)]^{1/2}, \tag{26}$$

where Δ and τ are the superconducting gap and the transmission coefficient of the junction, respectively, [31]. CPR is affected by the material between the

34

two SCs. Next, we discuss CPR for a short ballistic Josephson junction, which corresponds to the case in which the distance L between two SCs is less than the coherence length ξ of the superconductor and the mean free path l of the normal conductor. The short ballistic CPR is given by

$$
\begin{aligned}
I(\phi) = {} & \frac{e\Delta(T)}{2\hbar} \frac{\tau \sin(\phi)}{[1 - \tau \sin^2(\phi/2)]^{1/2}} \\
& \times \tanh\left(\frac{\Delta(T)}{2k_B T}[1 - \tau \sin^2(\phi/2)]^{1/2}\right),
\end{aligned}
\tag{27}
$$

where T is temperature [31–33]. Eq. (27) shows that CPR does not depend on L. Beenakker showed that $E > \Delta$ does not contribute to the CPR because the contribution $N(e\Delta/\hbar)L/\xi$ from this region becomes 0 when the short case $L/\xi \to 0$. Fig. 3 shows the case of short ballistic CPR. The CPR of Fig. 14 is highly skewed compared with the general sinusoidal CPR of $\sin\theta$. In particular, CPR becomes more skewed with larger τ and smaller T.
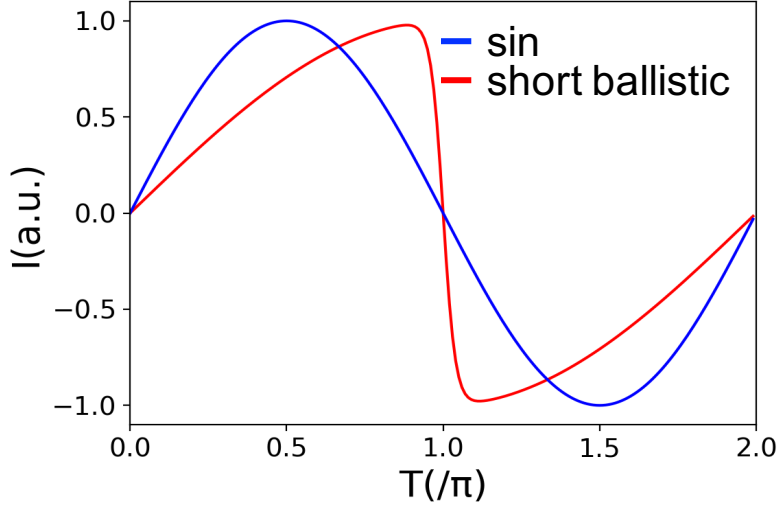
FIG. 14. Example of CPR of Josephson junctions: skewed CPR for the short ballistic Josephson junction (blue) and sinusoidal CPR for the standard Josephson junction (blue).

The short ballistic CPR was directly measured by Spanton et al. [34], who used an InAs NW. They fabricated an Al/ InAs NW/Al junction device, in which the contact between Al and InAs NW was epitaxially grown. The distance between the Al SCs was 150 nm, which is much shorter than the mean free path. This device was inductively coupled with a scanning superconducting quantum interference device (SQUID), which was used to measure the CPR directly. Fig. 15(a) is an optical microscopy image of the Al/InAs NW/Al junction connected with an Al ring. The size of the ring was adjusted to couple inductively to the pickup loop of the SQUID, which was utilized to measure the current flowing around the ring. The purple component is a field coil used to apply a phase difference between

the two SCs of the junction. The bottom gate of Au tunes the carrier density of a SNW. Fig. 15(b) shows a schematic illustration of the InAs NW (green) with epitaxial Al (blue) that are connected with an evaporated Al ring (grey). A typical example of the measured CPR is shown in Fig. 15(c). As theoretically predicted, the CPR indicated by the dotted line is skewed from the conventional sinusoidal function by the solid line.
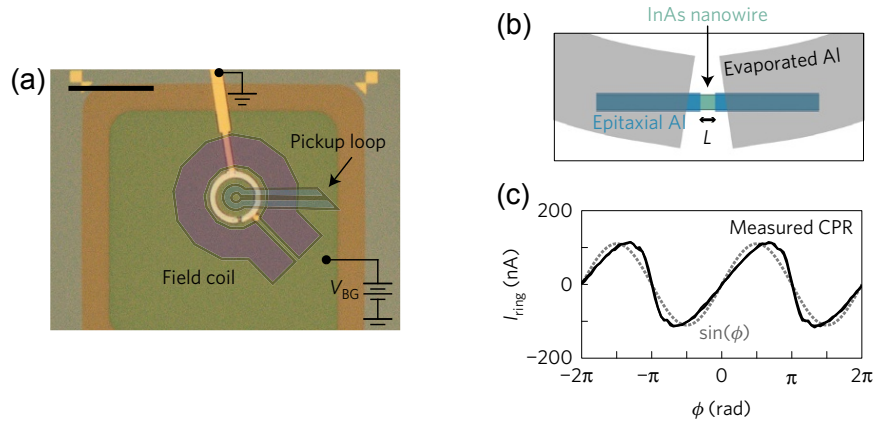
FIG. 15. (a) Optical microscopy image of a device consisting of an Al ring with a single epitaxial Al/InAs/Al junction. The blue component in the image is the SQUID pickup loop, and the purple component is a field coil [34]. (b) Schematic of the epitaxial Al/InAs NW/Al junction, where L is the distance between two epitaxial Al areas [34]. (c) The CPR indicated by the black curve is measured by an L = 150nm junction at the back gate $V_{BG} = 3.45$V and the temperature $T = 30$mK. The CPR has a non-sinusoidal shape, whereas the gray curve is a conventional sinusoid used as a reference [34].

37

D. RCSJ model

When a finite voltage V is applied to a Josephson junction, the time derivative of the phase difference ϕ between the two SCs evolves with time, as follows:

$$V = \frac{\hbar}{2e}\frac{d\phi}{dt} \tag{28}$$

The biased Josephson junction is represented by the equivalent circuit model (RCSJ model) of a resistively (R) capacitively (C) shunted Josephson junction [35, 36] (Fig. 17). The current flowing in this circuit is represented by Kirchhoff's law:

$$\frac{\hbar C}{2e}\frac{d^2\phi}{dt^2} + \frac{\hbar}{2eR}\frac{d\phi}{dt} + I(\phi) = I. \tag{29}$$

The solution of Eq. (29) yields the CPR $I(\phi)$ of the junction. On the other hand, the right-hand side of the equation that expresses I has DC and AC components, as follows:

$$I = I_{\text{dc}} + I_{\text{ac}}\sin(2\pi f t), \tag{30}$$

where $I_{dc}(I_{ac})$ and f are the applied DC (AC) current and the applied frequency, respectively. This equation is transformed into a dimensionless equation with $t' = (2eI_{\text{sw}}R)/\hbar \cdot t$, which is described as

$$\beta\frac{d^2\phi}{dt'^2} + \frac{d\phi}{dt'} + i(\phi) = i_{\text{dc}} + i_{\text{ac}}\sin(2\pi f't'). \tag{31}$$

Here, $\beta = 2eI_{\text{sw}}R^2C/\hbar$ is defined as the Stewart–McCumber parameter [35, 36] and $f' = f/2eI_{\text{sw}}R$. When $\beta \ll 1$, the Josephson junction becomes overdamped, and the $I - V$ trace is a smooth curve. In contrast, the Josephson junction is underdamped in the case of $\beta \gg 1$. In this case, the voltage jumps at a certain current value such that the $I - V$ trace exhibits hysteresis behavior.
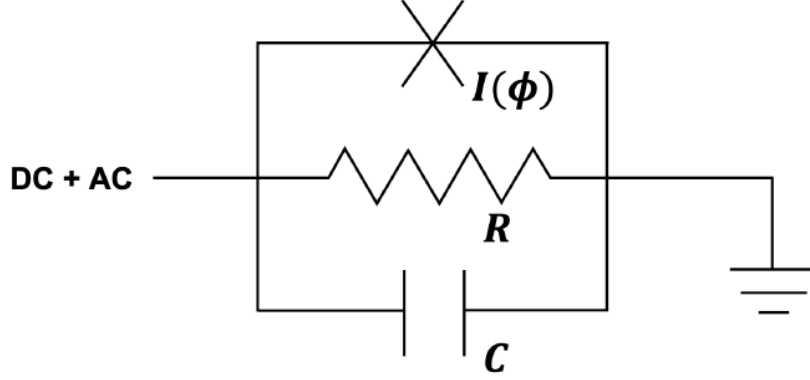
FIG. 16. RCSJ model. The DC and AC currents are applied not only to the Josephson junction, but also to the capacitance and resistance.

E.   Shapiro step

Although we studied the circuits driven by both the DC and AC components, it is mathematically easier to solve the case where an AC voltage is applied to the circuit. Substituting $V = V_0 + V_1 \cos(\omega t)$ into Eq.(28), the phase difference

$$\phi = \phi_0 + \frac{2e}{\hbar}V_0 t + \frac{2e}{\hbar\omega}V_1 \sin(\omega t). \tag{32}$$

The supercurrent becomes

$$I = I_c[\sin(\frac{2e}{\hbar}(V_0 t$$
$$+ \Delta\phi_0)\cos(\frac{2eV_1}{\hbar\omega}\sin(\omega t))) + \cos(\frac{2e}{\hbar}(V_0 t + \Delta\phi_0)\sin(\frac{2eV_1}{\hbar\omega}\sin(\omega t)]). \tag{33}$$

Using the formula

$$\exp(ia\sin(x)) = \sum_{k=-\infty}^{\infty} J_k(a)\cos(kx) + i\sum_{k=-\infty}^{\infty} J_k(a)\sin(kx), \tag{34}$$

39

Eq. (33) becomes

$$I = I_c \sum_{k=-\infty}^{\infty} (-1)^k J_k(\frac{2eV_1}{\hbar\omega}) \sin(\phi_0 + \omega t - k\omega t). \qquad (35)$$

Note that $J_k(a)$ is a Bessel function and $J_k(a) = (-1)^k J_{-k}(a)$. The supercurrent has the DC component $I = I_c(-1)^k J_k(\frac{2eV_1}{\hbar}) \sin(\phi_0)$ when

$$V_0 = n\hbar\omega/2e, (n = 0, \pm1, \pm2, \dots) \qquad (36)$$

When an AC current is applied, we have to solve the nonlinear second-order differential equation of Eq. (29). This is difficult to solve analytically. As a result, ladder behavior appears in the measurement of the DC current and the average voltage, referred to as Shapiro steps. The current jumps at the Shapiro steps [37]. The steps occur at voltages of $hf/2e$ ($n = 0, \pm1, \pm2, \dots$). This interval changes as a result of changes in various parameters: the CPR, the Stewart–McCumber parameter β, or the applied frequency.
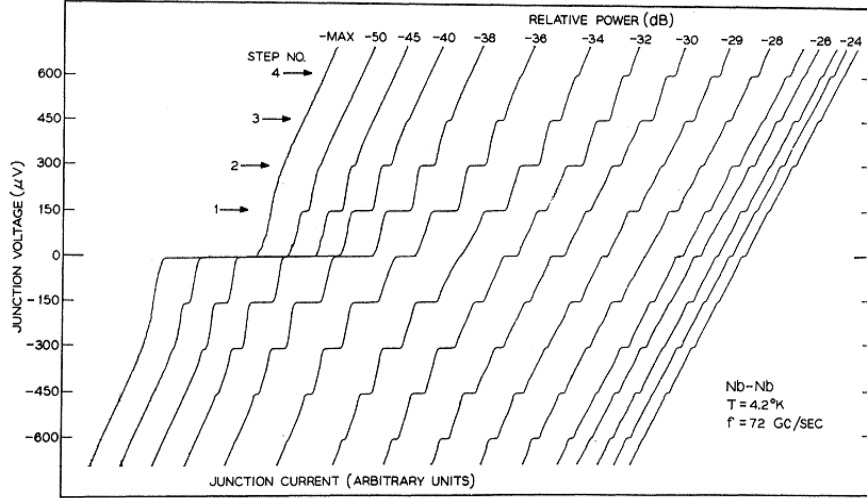
FIG. 17. Current-voltage curve for a Josephson junction under microwave irradiation at different powers, as measured by Grims and Shapiro [37].

Conventional CPR is represented by a sinusoidal function with a period of 2π. When a higher-order sinusoidal function is added, fractional steps also appear. In the presence of MBS, the period becomes 4π owing to the zero energy states [38], and the odd-numbered steps disappear. Even if CPR is only a sinusoidal function, if β becomes large, the behavior of the RCSJ model as an equation of motion changes and contributes to the generation of higher-order terms in the sinusoidal function, causing fractional steps [39]. When f becomes large, the quasiparticle is directly excised from the gap, inducing fractional steps [40–42]. (see the discussion in section 6-II-F.)

41

III.   Majorana Fermions

A.   General introduction

A Majorana fermion (MF), proposed by Ettore Majorana in 1937, is a special fermion that is its own anti-particle, and satisfies the following relation:

$$\{\gamma_i, \gamma_j\} = 2\delta_{ij} \tag{37}$$

B.   Kitaev model

Kitaev proposed a toy model of a spinless p-wave 1D SC, known as the Kitaev model [38]. The Hamiltonian is expressed as:

$$H = -\mu \sum_i c_i^\dagger c_i - \frac{1}{2} \sum_i (t c_i^\dagger c_{i+1} - \Delta c_i c_{i+1} + \text{h.c.}), \tag{38}$$

where μ, t, Δ, and c_i correspond to the chemical potential energy, nearest-neighbor hopping energy, superconducting gap energy of the spinless topological SC, and annihilation operator of the i-th fermion, respectively. In this model, the edge of the SC hosts the MFs. The i-th fermion is written as

$$c_i = \frac{1}{2}(\gamma_{B,i} + i\gamma_{A,i}) \tag{39}$$

$$c_i^\dagger = \frac{1}{2}(\gamma_{B,i} - i\gamma_{A,i}) \tag{40}$$

where γ_i is the operator of one MF, which forms the i-th fermion. One fermion consists of two MFs, indicated by indexes A and B, which satisfy the anticommutation relation of fermions (Fig. 18). Using this relation, Eq. (38) is rewritten as

$$H = -\frac{\mu}{2} \sum_i^N (1 + i\gamma_{B,i}\gamma_{A,i}) - \frac{i}{4} \sum_i^{N-1} [(\Delta + t)\gamma_{B,i}\gamma_{A,i+1} + (\Delta - t)\gamma_{A,i}\gamma_{B,i+1}]. \tag{41}$$

Here, the first term expresses the energy excited by one fermion, which is formed by two MFs. In the case of $t = \Delta = 0$, the second term becomes zero and only the first term remains, which is topologically trivial. In contrast, to consider the case of $-t < \mu < t$, which corresponds to a topologically non-trivial state, we assume $\mu = 0$ and $t = \Delta \neq 0$ for simplicity. We obtain the following equation from Eq. (41):

$$H = -i\frac{t}{2}\sum_{i}^{N-1}\gamma_{B,i}\gamma_{A,i+1} \tag{42}$$

This shows the combination of two MFs at different sites. Using a new definition of the fermion operator as $\tilde{c}_i = \frac{1}{2}(\gamma_{A,i+1} + i\gamma_{B,i})$, we transform Eq. (42) to

$$H = t\sum_{i}^{N-1}(\tilde{c}_i^\dagger\tilde{c}_i - \frac{1}{2}) \tag{43}$$

This shows that the MFs, which are $\gamma_{A,1}$ and $\gamma_{B,N}$ at both edges of the model, do not make any contribution. We can define an additional fermion operator from these non-local MFs.

$$f = \frac{1}{2}(\gamma_{A,i} + i\gamma_{B,N}). \tag{44}$$

Eq. 43 does not include any components of $\gamma_{A,1}$ and $\gamma_{B,N}$. Therefore, the anticommutation relation $\{f, H\} = 0$ is satisfied such that the ground state is degenerate. Additionally, one fermion exists at the edge as two MFs with zero energy. This is known as a Majorana zero mode. This fermion is formed by two non-local MFs, as shown in Eq. (44) and is not influenced by local perturbations. Therefore, using this fermion as the parity leads to a fault-tolerant quantum computer.
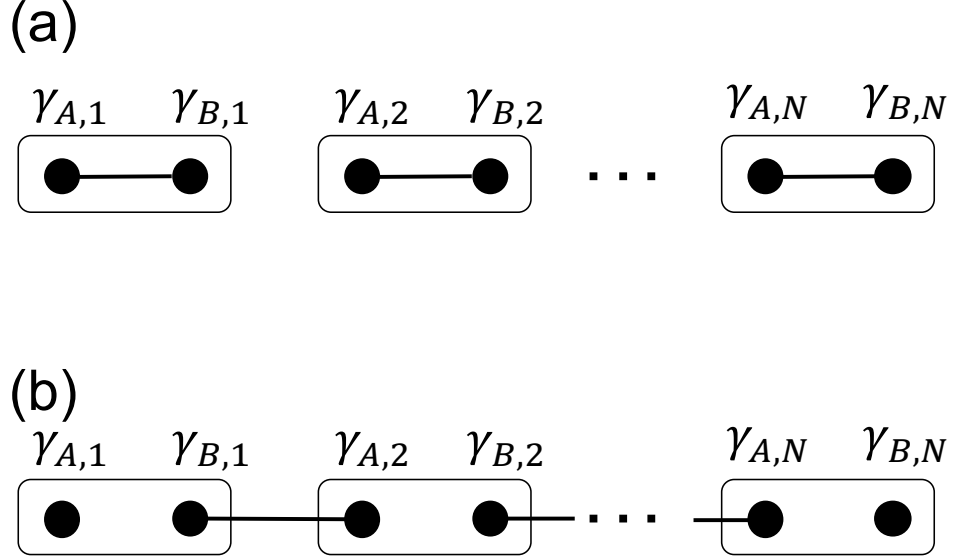
FIG. 18. (a) Topologically trivial state: Two MFs at the same site combine to form one fermion. (b) Topologically non-trivial state: Two MFs at different sites combine to form one fermion.

C.   How to realize the Kitaev model

Kitaev demonstrated the realization of a topological SC in a spinless p-wave 1D SC. Interestingly, a hybrid device consisting of a NW with a strong spin-orbit interaction (SOI) and an s-wave SC exposed to a magnetic field [43, 44] is considered to be a spinless p-wave SC, such that MFs emerge at the edge of the device [43].

Let the wire lie along the x-axis, the spin-orbit interaction, α, be along the z-axis, and a magnetic field B is applied along the y-axis (Fig. 20(a)). The wire
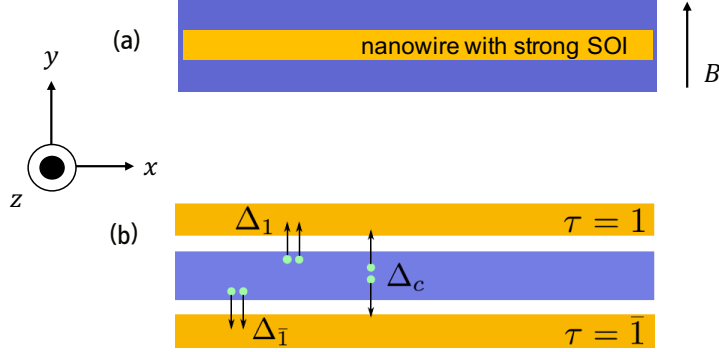
FIG. 19. (a) Schematic of a hybrid device spin-orbit-coupled NW (yellow) with an s-wave SC (blue). (b) Schematic of two 1D quantum wires (yellow), which have a strong Rashba SOI coupled to an s-wave SC (blue). The intrawire proximity-induced superconductivity of Δ_τ illustrates Cooper pair tunneling into the τ wire ($\tau = 1, -1$). In contrast, the interwire proximity-induced superconductivity of Δ_c illustrates the CAR into both wires [45].

is proximitized with a superconducting gap energy Δ. The Hamiltonian is

$$H = \int \Psi^\dagger(x)\mathcal{H}\Psi(x)dx \tag{45}$$

$$\Psi^\dagger = (\Psi_\uparrow^\dagger, \Psi_\downarrow^\dagger, \Psi_\downarrow, -\Psi_\uparrow) \tag{46}$$

$$\mathcal{H} = [p^2/2m - \mu]\tau_z + \alpha p\sigma_z\tau_z + B\sigma_x + \Delta\tau_x, \tag{47}$$

Here, $\psi_\sigma^\dagger$ is a creation operator with effective mass m, chemical potential μ, and Pauli matrix σ, τ in spin and particle-hole space. $\alpha > 0$ denotes the strength of spin-orbit coupling along or against the x-direction. In the absence of either a magnetic field or a superconducting gap, the Hamiltonian has only the Rashba spin orbital interaction. As a result, the energy spectrum takes the form of two shifted parabolas, which cross at $p = 0$. When a magnetic field and a supercon-

ducting gap are introduced, the energy spectrum is

$$E_\pm^2 = B^2 + \Delta^2 + \xi_p^2 + (\alpha p)^2 \pm 2\sqrt{B^2\Delta^2 + B^2\xi_p^2 + (\alpha p)^2\xi_p^2}, \qquad (48)$$

where $\xi_p = p^2/2m - \mu$. The key point to host MFs is the $p = 0$ energy gap E_0. The energy is

$$E_0 = |B - \sqrt{\Delta^2 + \mu^2}|. \qquad (49)$$

At $B^2 = \Delta^2 + \mu^2$, the topological transition occurs. As B increases, the wire is in the topological phase for $B^2 > \Delta^2 + \mu^2$, with MBSs at the wire ends. A considerable amount of research has been conducted, and much evidence for the existence of MFs has been presented [3–5, 8, 46, 47].

D. MFs and parafermions in a double nanowire system

MFs are expected to find application in topological quantum computers [10, 48]. However, they do not satisfy the necessary conditions for universal quantum computation [49]. On the other hand, Fibonacci anyons might be a candidate for the realization of a universal quantum computer [49, 50]. Parafermions (PFs) of Fibonacci anyons, referred to as fractional MFs, have the potential for more universal quantum operations than MFs. In contrast to MFs, PFs require strong electron–electron interactions. The most well-known theoretical proposals to host PFs are on edge states of fractional quantum Hall effect (FQHE) systems proximitized by an SC [51]. However, the disadvantage of these systems is the same as that of a hybrid device consisting of an SC and semiconductor NW to host MFs. It is necessary to apply a strong magnetic field to the system to realize the FQHE, which has a negative effect on the superconductivity [52].

Recently, a theory that holds in the absence of a magnetic field was proposed [45, 53]. The proposed platform for the realization of PFs is illustrated in Fig. 20. We prepared two 1D quantum wires with Rashba strong SOI. They are coupled to an s-wave SC, which induces proximitized superconductivity. This system contains two pairing terms. The first is the intrawire proximity-induced superconductivity of $\Delta_{1(\bar{1})}$, which corresponds to the Cooper pair tunneling of two incident electrons on each wire. The other is the interwire SC of Δ_c induced by the CPS, which is equal to the CAR on both wires. The interwire-induced energy Δ_c is more dominant than the intrawire energy $\Delta_{1(\bar{1})}$ in the regime of strong electron–electron interaction. In this case, the system becomes topologically non-trivial, such that MFs or PFs are localized at the edges of the 1D system. If the chemical potential energy is tuned to the Kramers point of the spectrum, the 1D system hosts two MFs, which are a time-reversal of each other at the edge of the system. Furthermore, decreasing the chemical potential to one-ninth of the SOI energy such that the electron–electron interaction is strengthened has the effect of hosting $\mathbb{Z}_3$ PFs as the zero energy state in the system.

We consider a system of two quantum wires with a strong Rashba SOI that is induced by an s-wave SC in Fig. 20, following Ref. [45]. The upper (lower) wire parallel to the x-direction is labeled as $\tau = 1$ ($\tau = \bar{1}$). The Hamiltonian of this model is described by:

$$H = H_0 + H_{SO} + H_S + H_c + H_Z. \tag{50}$$

The Hamiltonian consists of five parts. The first term of Eq. (50) is the kinetic part, given by

$$H_0 = \Sigma_{\tau,\sigma} \int dx \Psi_{\tau\sigma}^\dagger(x)[\frac{-\hbar^2\partial_x^2}{2m} - \mu_\tau]\Psi_{\tau\sigma}(x), \tag{51}$$

where $\Psi_{\tau\sigma}^\dagger(x)[\Psi_{\tau\sigma}(x)]$ is the creation (annihilation) operator of an electron of mass
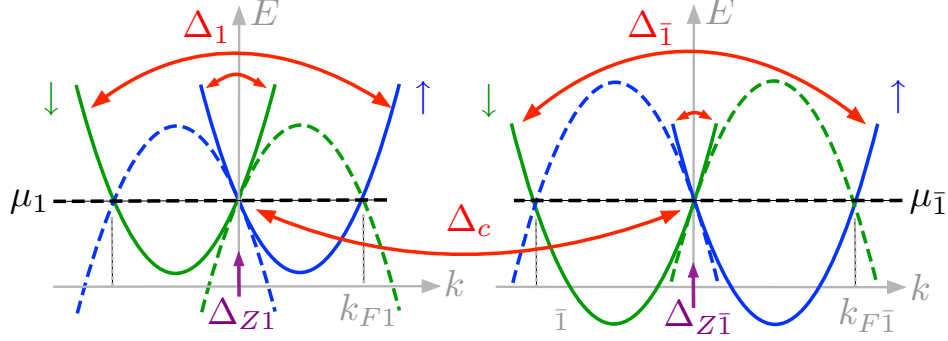
47

FIG. 20. Spectrum of two wires with a positive (negative) Rashba SOI for $\tau = 1 (\tau = \bar{1})$ [54]. The solid (dashed) lines represent the spectra of electrons (holes), and the blue (green) lines correspond to spin-up (spin-down). It is necessary to tune the chemical potential to the crossing point between the blue and green lines, which is known as the Kramers point. The term $\Delta_c (\Delta_\tau)$ is the proximity-induced superconductivity of different (same) wires. The spectrum becomes gapless for $\Delta_c = \Delta_1 \Delta_{\bar{1}}$, which results in a topological transition. In the topological phase, two MFs are localized at the edge of one quantum wire, such that four MFs exist in the system. In this case, the interwire superconductivity of Δ_c couples states with $k = 0$.

m at position x of the wire τ with spin $\tau/2$ along the z-axis, and μ_τ is the chemical potential. The second term is the energy caused by Rashba SOI. The Rashba SOI field, $\alpha_{R\tau}$, determines the strength and direction of the spin polarization. Thus, this term is described as

$$H_{SO} = -i\Sigma_{\tau,\sigma,\sigma'} \alpha_{R\tau} \int dx \tau \Psi_{\tau\sigma}^\dagger(x) (\sigma_3)_{\tau\tau'\ prime} \partial_x \Psi_{\tau\sigma'}(x). \tag{52}$$

Here, the Pauli matrices $\sigma_{1,2,3}$ act on the spin of the electron. The third component is the Hamiltonian of the intrawire superconductivity of strength Δ_τ, which is the

48

proximity induced in each quantum wire by Cooper pair tunneling from the SC to the wire τ. This Cooper pair consists of spin-up and spin-down electrons at $k = 0$ or $k = \pm K_F$. The intrawire term is written as

$$H_S = \Sigma_{\tau,\sigma,\sigma'} \int dx \frac{\Delta_\tau}{2} [\Psi_{\tau\sigma}(i\sigma_2)_{\sigma\sigma'} \Psi_{\tau\sigma\ prime} + \text{h.c.}].\tag{53}$$

The fourth part is due to CPS, which occurs if the distance between two quantum wires is shorter than the coherence length of an SC in contact with the quantum wire, which results in interwire proximity-induced superconductivity.

$$H_C = \Sigma_{\tau,\sigma,\sigma'} \int dx \frac{\Delta_c}{2} [\Psi_{\tau\sigma}(i\sigma_2)_{\sigma\sigma'} \Psi_{\bar\tau\sigma'} + \text{h.c.}],\tag{54}$$

where Δ_c is the energy of the interwire proximity-induced superconductivity, which is coupled at $k = 0$. Therefore, CPS is more dominant than Cooper pair tunneling when $\Delta_c > \Delta_\tau$. The last part of the Hamiltonian is

$$H_Z = \Sigma_{\tau,\sigma,\sigma'} \Delta_{Z\tau} \int dx \Psi^\dagger_{\tau\sigma}(\sigma_x)_{\tau\tau'\ prime} \Psi_{\tau\sigma},\tag{55}$$

where $\Delta_{Z\tau} = g_\tau \mu_B B/2$ is the Zeeman splitting in the τ-wire with the magnetic field along the x-axis. In the absence of a magnetic field, CPS couples the branches of the energy spectrum to close the gap and induces a topological transition at $k = 0$ if $\Delta_c^2 = \Delta_1 \Delta_{\bar 1}$ and $k = \pm 2\sqrt{\Delta_c^2 - \Delta_1^2}/\hbar v_F$ if $\Delta_1 = \Delta_{\bar 1} < \Delta_c$. If $\Delta_c^2 > \Delta_1 \Delta_{\bar 1}$ and $\Delta_1 \neq \Delta_{\bar 1}$, the two zero-energy states are localized at the left edge, and the two states are at the right edge of the system. These two bound states on the one side engage in Kramers-pairing with each other by time-reversal symmetry (see the details in [45, 53, 54]). We note that the topological transition occurs if the interwire superconducting energy is equal to the sum of the intrawire superconducting energy and the Zeeman splitting. If we do not take Δ_c into account, the magnetic field couples the states of opposite spin in each NW, similar to the SNW system in III-C.

Chapter 3

Preceding studies

I.   Previous experiments with ballistic nanowire devices

A wide variety of experiments have been conducted using semiconductor
NWs [55–58].   These NWs are 1D conductors, ranging from those that take
advantage of their 1D nature to those that utilize the formation of dots in NWs.
In particular, improving the quality of the NWs and ensuring good contact with
the electrodes leads to the observation of ballistic properties. In this section, we
introduce experiments in which the ballistic properties of NWs are observed.

A.   Ballistic conductance of nanowires

The formulation of 1D subbands results in the conductance quantization of
NWs. However, the observation of ballistic transport with conductance quantiza-
tion is rarely reported because it is difficult to fabricate high-quality NWs with
good contacts to the electrodes. Electron scattering occurs when electrons conflict
with impurities in the NW and diffusively reflect at the surface. In particular,
the physical phenomenon where electrons scatter backward is known as backscat-
tering, which is one of the reasons for the difficulty in observing the conductance
quantization. This is because there is little freedom of electron's forward move-
ment in the NW rather than in a quantum point contact in a two-dimensional
electron gas (Fig. 21). Another important point is the contact between the NWs
and their electrodes. Electrons can also be scattered at the interface. If the inter-

face is of good quality, the electron transmittance will be close to unity, and the quantized conductance appears as plateaus of multiples of e^2/h. To date, several transport experiments have been performed for NWs consisting of InAs or InSb. For the InAs NWs, conducting electrons are accumulated in the surface inversion layer. Therefore, good electrical contacts can be formed with metal electrodes but the electron transport is more severely affected by the surface states. On the other hand, for the InSb NWs, electrons are confined inside the NW. Therefore, the transport is not affected by the surface states but more careful surface treatment is required to form good contacts with the electrodes. In this work, we are concerned about the interface quality between the NW and SC, and therefore used InAs NWs and made efforts to clean the NW surface as much as possible. Thus, to observe ballistic NWs showing quantized conductance was an important task. Below we review previous experimental efforts to prepare such ballistic NWs.
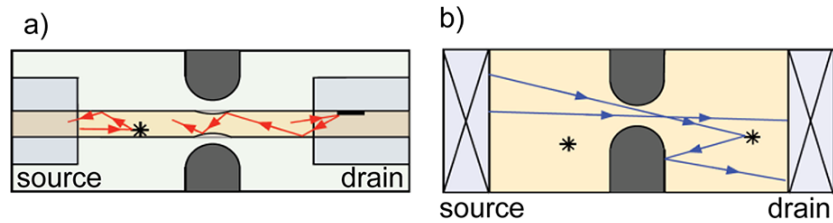

FIG. 21. Schematic of electron transport for the case of a 1D channel of the NW in (a) and a constriction formed in a two-dimensional electron gas in (b) [59]. Electrons conflict with impurities and reflect if they exist on the route of electron transport in (a). Compared with (a), the effect of electron scattering in the two-dimensional case is less than that in (b).

Fig. 22(a) shows an SEM image of a device of an InAs NW and nickel as

51

electrodes [60]. ZrO_2 is deposited on the NW as a top-gate Vgs structure using atomic layer deposition (ALD). Fig. 22(b) shows the conductance as a function of the gate voltage measured at various temperatures. The first and second conductance plateaus are clearly visible at 120 K and become blurred as the temperature increases. These conductance plateaus are more clearly defined in InSb NWs [59, 61]. Fig. 22(c) shows an SEM image of an InSb device with source-drain contacts of Cr/Au and a top gate of Ti/Au [61]. Fig. 22(d) shows that the first conductance plateau is well defined at zero-magnetic field and changes to spin-split plateaus with increasing magnetic field.
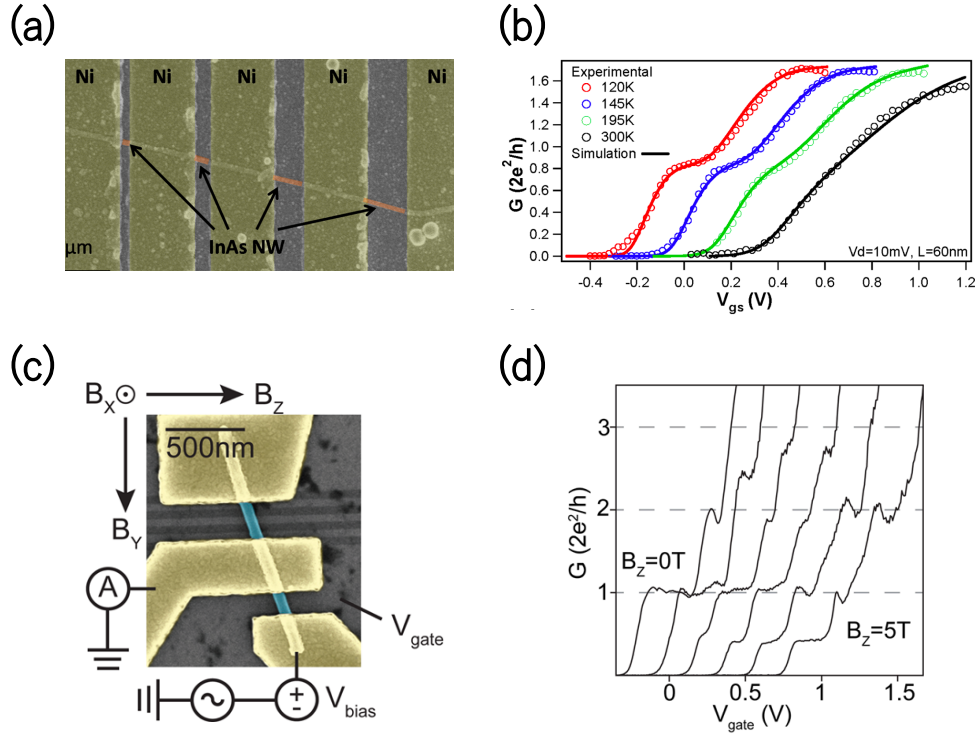
FIG. 22. (a) SEM image of an InAs-Ni device [60]. (b) Temperature dependence of the $G - V_{gs}$ plots. The plots are shifted for clarity [60]. (c) SEM image of an InSb-Au device [61]. (d) V_{gate} dependence of the conductance from 0 T to 5 T. Each curve is offset by 200 mV [61].

B. Supercurrent in InAs nanowire device

Improving the quality of NWs and forming a clean contact between the NWs and SC are particularly important to observe the supercurrent flow. Observation of the quantized conductance allows the number of 1D channels in the NW to be defined; thus, it is theoretically predicted that the value of the critical supercurrent

increases by $e\Delta/\hbar$ with the number of channels [62], where Δ is the proximitized superconducting gap of a SC-NW-SC device. Many reports on the supercurrent in NW devices have been published [56, 58, 63, 64]. Here we introduce one of them [58]. The sample of Al - InAs NW - Al has a cross-linked structure, and the carrier density of the device was tuned by a back gate electrode (Fig. 23(a)). The diameter and length of the NWs were 80 nm and 4 μm, respectively. Fig. 23(b) shows the change in conductance as a function of the back gate voltage V_g and junction voltage V. The conductance is higher inside the superconducting gap than outside, and is characterized by the two lines at $V = \pm\Delta/e$. The number of channels in the NW increases with V_g because the potential barriers in the NW become small. The conductance plateaus measured outside the gap are not quantized at multiples of e^2/h. This difference is due to the transmission of less than unity. In addition, the enhancement of the conductance inside the superconducting gap is attributed to the contribution of two electrons in the mechanism of AR. Next, the supercurrent measured as a function of V_g is shown in Fig. 24(b). The supercurrent starts to flow above the pinch-off voltage $V_g = -0.8$ V. Although the supercurrent increases with more channels, the value of the supercurrent is not stable to form a plateau, and is smaller than theoretically expected. In fact, the electrons scatter due to the presence of impurities in the NWs, such that the supercurrent oscillates in plateaus. In addition, the SOI of the InAs NW must be considered to analyze the values of the supercurrent more accurately.
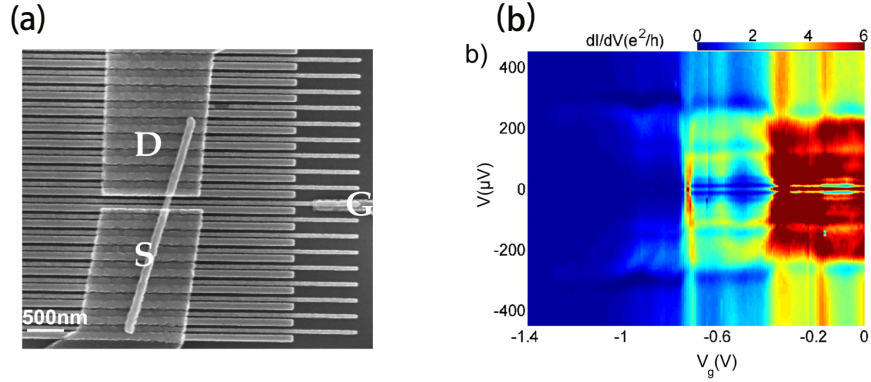
FIG. 23. (a) SEM image of the Al-InAs NW-Al sample. A back gate of Ti/Au controls the carrier density of InAs NWs [58]. (b) Differential conductance as a function of V_g and V at $T = 15$ mK [58].
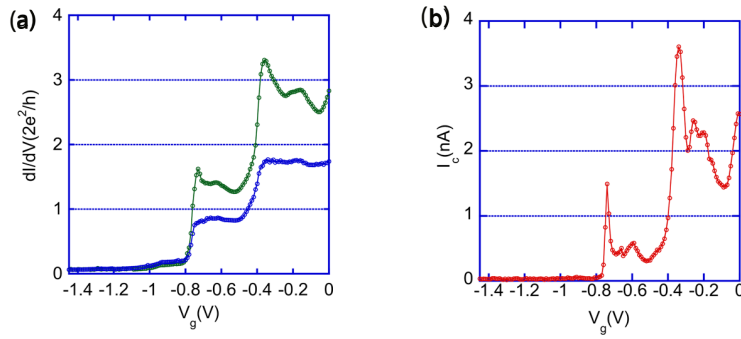

FIG. 24. (a) Differential conductance as a function of V_g in the normal (superconducting) state, in blue (green). The Andreev reflection results in an enhancement of the conductance in the superconducting gap [58]. (b) Supercurrent as a function of V_g. The supercurrent increases with V_g. However, the value of the supercurrent in the plateau of (a) is not constant, but oscillates [58].

55

II.   observation of Majorana fermion

A large amount of research has been conducted, and quite a few experiments have claimed the observation of MBSs in hybrid devices with InAs or InSb NWs [3–5, 8, 46, 47]. The first experiment was performed using a normal metal (Au) - InSb NW - SC (NbTiN), shown in Fig. 25(a). The InSb NW has a large g-factor and strong SOI, both of which favor the generation of MFs at each end of the SC (see III-C). Fig. 25(b) shows the differential conductance measured as a function of the source-drain voltage V and magnetic field B. A conductance zero-bias peak is observed at a finite magnetic field, which is attributed to the formation of MBSs. Soon afterwards observation of a similar zero-bias peak was reported using an InSb NW [5] and an InAs NW [4](Fig. 25(c) and (d), respectively). Note that it has recently been debated that measurement of the zero-bias anomaly is not sufficient to solidify the presence of MFs for other reasons such as ABS [65–67].

Several types of experiments to indicate the presence of MBSs have been proposed. Among the proposed experiments is the exploration of the Shapiro steps. As described in II-E, in the presence of MFs, the phase periodicity of the Josephson junction of the topological superconductor is modified from 2π to 4π. This predicts the vanishing of the odd-numbered Shapiro steps. An experiment on this prediction was carried out for a Josephson junction having an etched constriction formed in an InSb quantum well [8]. The first Shapiro step was observed to vanish, as shown in Fig. 26. Similar but more definite experiments on the vanishing Shapiro-steps were later performed using the HgTe topological insulator Josephson junctions [9].
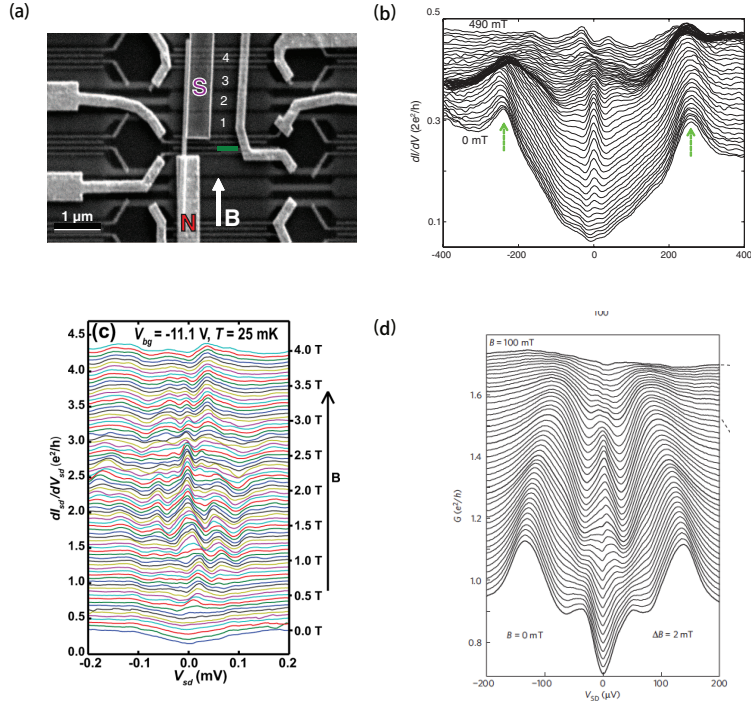
FIG. 25. (a) SEM image of the device in (b). The device is a superconductor (NbTiN) - InSb NW - a normal conductor (Au) junction [3]. (b) Differential conductance dI/dV against V at $T = 70$ mK. Applying B results in a conductance peak at zero bias attributed to MBS [3]. (c) Differential conductance at $T = 25$ mK from $0 - 4$ T using a Nb-InSb NW device. The conductance peak emerges when B exceeds 1 T [5]. (d) Differential conductance at $T = 30$ mK from $0 - 1$ T using an Al-InAs NW device. The conductance peak emerges at values larger than 100 mT [4].

Another way to detect MFs was proposed in the same year. In the presence of MFs, the periodicity of the Josephson junction of the topological superconductor is modified from 2π to 4π. As a result of the novel periodicity, the odd integer of
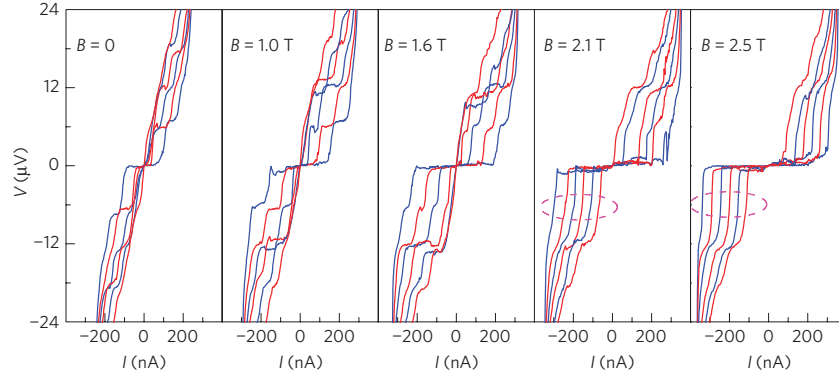
57

the Shapiro steps vanishes in Fig. 26 [8].

FIG. 26. Measurement of the Shapiro steps of an InSb - Nb hybrid device. $I - V$ characteristics under microwave irradiation. The first plateau of the Shapiro steps disappears as a result of the topological transition for $B > 2.1$ T [8].

Chapter 4

Sample fabrication

I. Fabrication of Josephson junction devices

The NW Josephson devices were fabricated by first identifying good candidates for SNW and DNW among a number of InAs NWs. Then, a pair of closely spaced Al electrodes were positioned and placed over the SNW (or DNW), and finally, a top or side gate (or two top or side gates) were placed as close as possible to the SNW (DNW). The processing details are described below.

A. Preparation of InAs single nanowire and double nanowire

The InAs NWs used in this research were grown by chemical beam epitaxy (CBE) in Prof. Xu's group of Lund University [68, 69]. The use of CBE requires the deposition of pure gold particles on a substrate as seeds from which to grow the NWs. The typical lengths of the NWs fabricated in this way range from 1 μm to 4 μm, with diameters from 60 nm to 80 nm. First, we have to place markers on the substrate to accurately position each NW. The markers consist of Ti/Au. The thickness of the markers should preferably be approximately the same as the diameter of the NWs because this is convenient for subsequent AFM or SEM analyses as it would enable the samples to be clearly visualized. Before transferring the NWs, we have to clean the substrate of SiO$_2$/Si used for NW devices. We first dipped the substrate in acetone for 5 min to remove impurities. Second, we placed the substrate on a heater at 180 °C for 5 min. Finally, we

used oxygen plasma to remove residues from the substrate surface. The next step after cleaning the surface entailed transferring the NWs from the growth substrate to the device substrate. We selected a large number of NWs from the growth substrate using a cotton wool bud (Fig. 27(a)(i)) and transferred them to the device substrate (Fig. 27(a)(ii)). In the case of the DNW experiment, it is important to choose two adjacent NWs that are aligned parallel to each other. This was accomplished by accurately locating the NWs using an optical microscope, AFM, and SEM. After transferring the NWs, we used the optical microscope to determine how many NWs, especially DNW are on the substrate and to locate them before using AFM or SEM. SEM (Fig. 27(b)) has a higher resolution than AFM, which allows for a higher degree of alignment; however, a critical disadvantage exists. The SEM electron beam damages the NWs and degrades their transport properties. Therefore, we accurately located the position of NWs that are suitable for measurement using AFM instead of SEM.

B. Fabrication of superconducting contacts and gate electrodes

Immediately after preparing the NWs, we deposited Ti/Al (1.5 nm/100 nm) as the superconducting contacts using an e-beam lithography technique. Before the contacts were deposited, it was necessary to treat the surfaces of the NWs. Electron beam processing requires the use of PMMA as a resist, which was developed in the solution MIBK:IPA = 1:2 for 60 s. Next, we removed PMMA residues by reactive ion etching (RIE, 30 W and 10-30 s), after which the native surface oxide components of the NWs were removed by etching them in a $(NH_4)_2S_x$ solution ($H_2O : 20\%$, $(NH_4)_2S_x = 10 : 1$) for 120 s at 40 °C. Finally, we added gate electrodes to tune the carrier density in the NWs. For this purpose, we initially

attempted to fabricate side gates near the NWs but on the same plane. However, with this arrangement it is challenging to tune the carrier density because it is difficult to maintain a short distance between the NWs and the side gates with the e-beam lithography process. Therefore, we changed our plan and adopted top gate structures. We covered the NWs and Al contacts with a 40-num thick Al_2O_3 layer grown by ALD [1, 27, 29, 70], and then deposited Ti/Au on top of the NWs as top gates.

C.   DNW and SNW Josephson junction devices

Fig. 28 (a) and (b) show an SEM image of the fabricated DNW Josephson device without and with gate electrodes, respectively. The DNW device has two SC electrodes separated by approximately 20 nm. We note that the device in the image is different from the measured device because we refrained from using SEM to avoid damage to the NW device. Fig. 28(c) shows a schematic of the DNW Josephson device with two top gates, g1 and g2. These gates can be used to control the conductance of the two respective NWs, NW1 and NW2, respectively. Fig. 29 shows an SEM image of the single InAs NW Josephson junction device. The junction length between the two SCs in blue is approximately 100 nm. A single to gate in brown covers the entire NWs in the junction and parts of the SC contacts. This gate can be used to efficiently change the carrier density of the NWs.
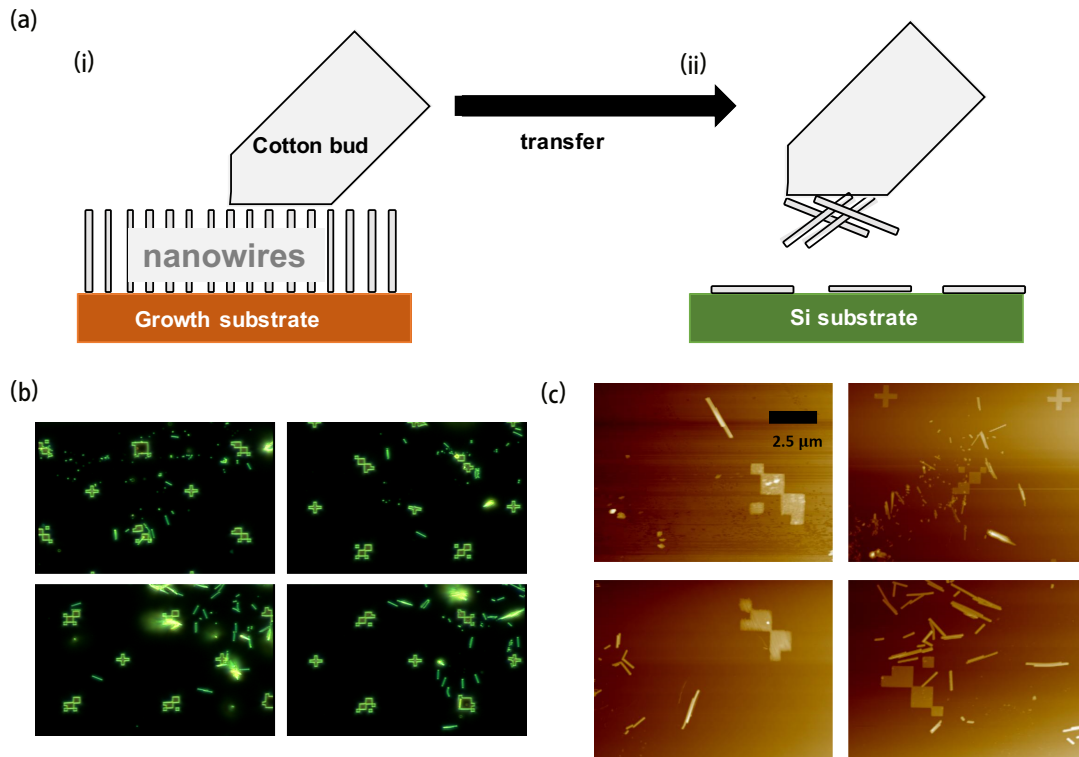
FIG. 27. NW transfer process. (a)(i) Many NWs are gathered using a cotton wool bud. (ii) They are transferred to the device substrate by touching the substrate with the cotton wool bud. (b) SEM image of the NWs. (c) AFM image of the NWs.
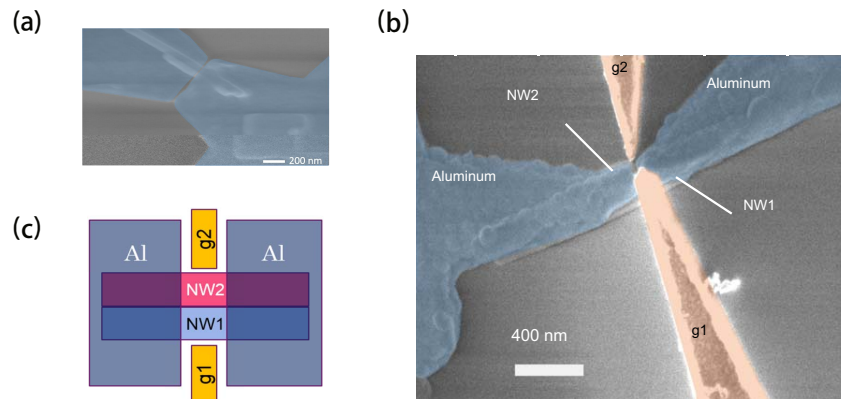
FIG. 28. (a) SEM image of a device that differs from that used for measurements. Two Al electrodes were deposited on the DNW. The distance between two contacts was approximately 30 nm [1]. (b) SEM image of the device with two Al electrodes (blue) in contact with the DNW. Two top gates (orange) were deposited on the DNW [1]. (c) Schematic of the devices NW1 and NW2 tuned by the top gate electrode g1 with V_{g1} and g2 with V_{g2}, respectively, [1].
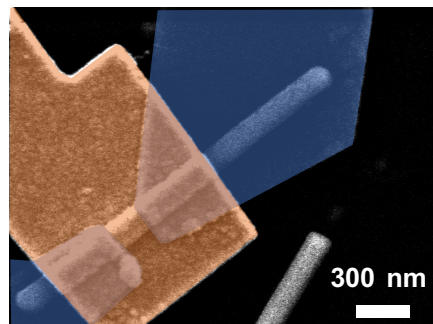

FIG. 29. SEM image of an InAs NW with a top gate structure (orange). This device in the image differs from that used for measurements in this study. The junction length between the two Al areas (blue) was approximately 100 nm [2].

II. Measurement system

We employed a standard lock-in technique and measured the DNW sample in a dilution fridge (K400, Oxford Instruments). For the SNW sample, we performed standard constant voltage and constant current measurements in a dilution fridge (MX50, Oxford Instruments). The setup required for the measurement of the Shapiro step is shown in Fig. 30(a). Microwave is irradiated onto the sample through a semirigid cable placed just on top (Fig. 30(b)). We incorporated attenuators because the direct application of high frequency from the generator to the sample was too powerful. The applied frequency was set to 1–5 GHz to avoid affecting the measured temperature and the nonadiabatic effect caused by the high applied frequency (see Chapter 2-Ⅱ-E). To reduce the noise in the measurement, we prepared a copper block, a copper ribbon, and a NbTi coaxial cable (Fig. 31). Copper is the most reliable material for shielding from radio frequencies because it absorbs and attenuates both magnetic and radio waves. NbTi coaxial cables have extremely low thermal conductivity and are not affected by a strong magnetic field.
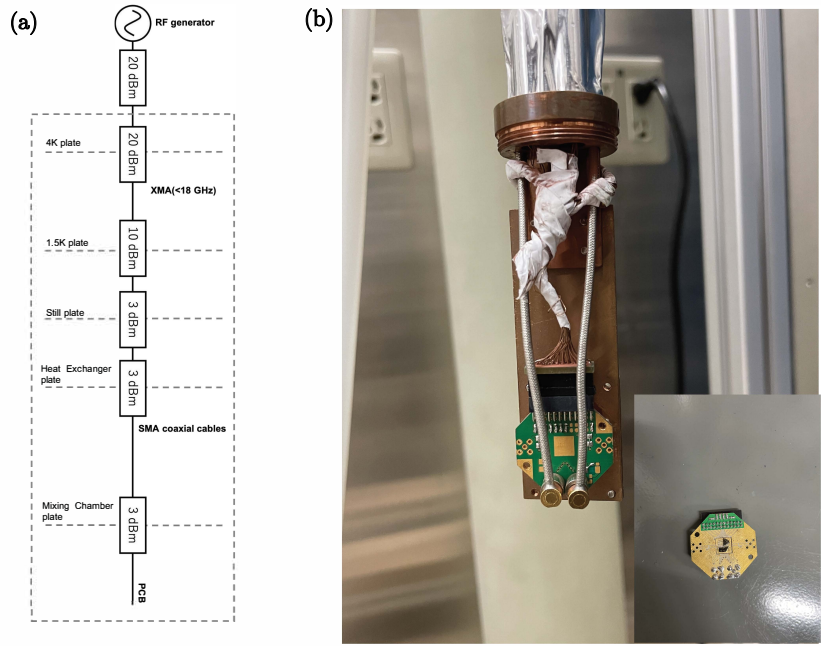
FIG. 30. (a) RF setup for measurement of the Shapiro step. (b) PCB board connected with semirigid RF cables. Inset:PCB board. Samples are set in the center of the PCB board.
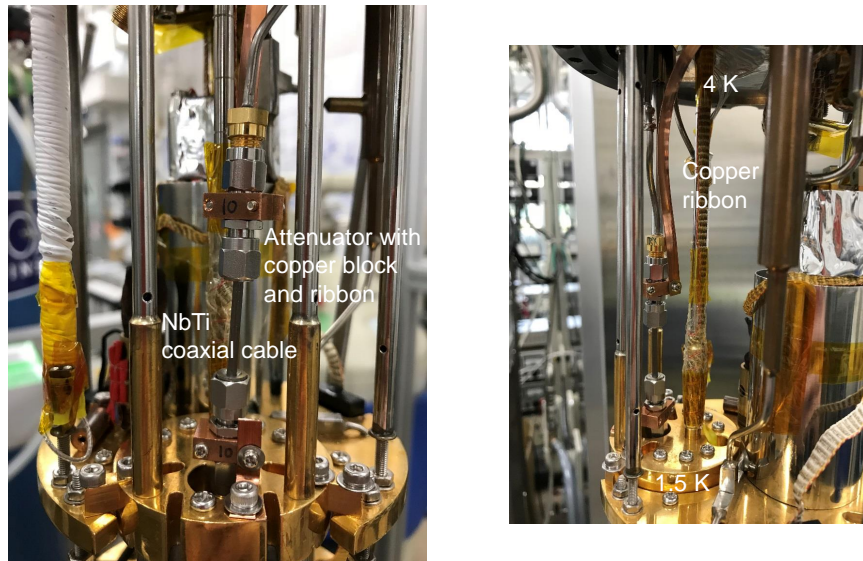
FIG. 31. Thermal anchor. NbTi coaxial cables and copper block and ribbon were used to reduce the noise of the thermal effect, magnetic field, and radio waves.

Chapter 5

Observation of CPS in ballistic double nanowire systems

I. General introduction

CPS has been demonstrated using QDs formed in SNW and parallel double NW (DNW) systems, but experiments in 1D systems have not yet been performed. The realization of CPS in 1D systems enables us to transport and manipulate Cooper pairs more effectively because the freedom of electron's motion increases. In addition, a theory exists that the realization of CPS in 1D conductors leads to topological transitions without any magnetic field, generating MFs at the edge of the system [45, 54, 71–73]. In our group, we studied techniques to fabricate DNW and used these DNW to conduct CPS experiments. In this chapter, we demonstrate the CPS in a 1D system of DNW using supercurrent measurements [1]. We discovered that the measured switching current to the two separate NWs was significantly higher than the sum of the switching currents to each of the NWs, indicating that the interwire superconductivity is dominant over the intrawire superconductivity. This satisfies the necessary condition for engineering MFs in the absence of a magnetic field.

II.   Measurement results

A.   Normal state conductance property

The device in Fig. 28 was measured in a dilution refrigerator at 50 mK $-$ 4 K. We used a standard lock-in technique to measure the differential conductance and supercurrent of the device.

First, we measured the differential conductance G of the Josephson junction device by applying a strong magnetic field $B = 250$ mT, which exceeds the critical field of Al. Fig. 32(a) shows G as a function of two voltages V_{g1} and V_{g2} for g1 and g2 to show the normal state transport of the device. The region below the blue solid line and to the left of the red solid line is the area in which both NW1 and NW2 are pinched off. The conduction areas are divided into four regions separated by the blue and red lines: a SNW to the conduction through each SNW (upper left for NW1 lower right for NW2), contribution of the DNW to conduction through the DNW (upper right), and no conduction (lower left).

Fig. 32(b) shows certain sections of the conductance line from Fig. 32(a). The blue (red) lines correspond to G in the SNW region of NW1 (NW2), measured by setting V_{g2} between -5.0 and -8.0 V (V_{g1} between $-$ -17.0 and $-$ -20.0 V). A quantized plateau-like structure was observed for $G = ne^2/h$ ($n = 2, 4, 6$). Typical data of the quantized conductance are shown in bold lines. The oscillations near the plateau are due to the scattering of impurities. The observation of the quantized conductance proves that our device is ballistic.

Therefore, G in the DNW region (upper right) is given by $G(m, n) = me^2/h + ne^2/h$, where m and n are the number of channels of NW1 and NW2, respectively. We define this (m,n) region as (m,n).

Next, we focused on electron conduction in the DNW region. Fig. 32(c) shows G from the purple line in Fig. 32(a). This purple line is on (0,0),(2,2), and (4,4). Fig. 32(c) explains this well, because quantized plateaus appear at $G = 4e^2/h$ and $8e^2/h$. As in the previous statement regarding the SNW region, we confirmed that the DNW are ballistic, and the conductance in the normal state represents the sum of the independent conductance of the two respective NWs.
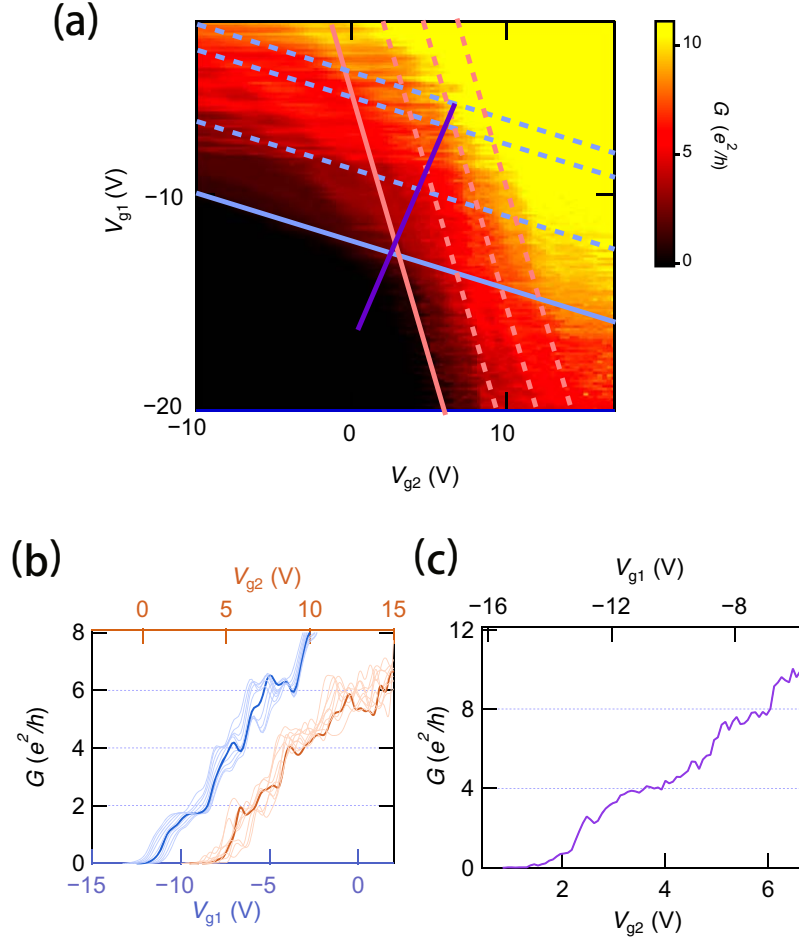
FIG. 32. Differential conductance G normalized by e^2/h as a function of V_{g1} and V_{g2} [1]. (a) G in the normal state as a function of V_{g1} and V_{g2} for $B = 250$ mT and $T = 50$ mK. The solid blue and red lines are along the NW1 and NW2 pinch-off areas. The dashed lines parallel to the solid lines are transition lines between the respective NW plateaus. (b) G vs. V_{g1} (blue) in the range from $V_{g2} = -5.0$ V to $V_{g2}-8.0$ V, where NW2 is pinched off, and G vs. V_{g2} (red) in the range of $V_{g1} = -17.0$ V to $V_{g2} - 20.0$ V, where NW1 is pinched off. All the curves have plateau-like structures at $G = 2e^2/h$, $4e^2/h$, $6e^2/h$. (c) G plotted along the purple line of (a), where both NW1 and NW2 contribute to the conduction of the device. The conductance plateaus are observed at $4e^2/h$ and $8e^2/h$.

B.   Estimation of the superconducting gap

We studied the superconducting properties of the Josephson junction device in the absence of the magnetic field. We measured G as a function of the bias voltage V_{sd} at $V_{g1} = -9.94$ V and $V_{g2} = -8.19$ V in the SNW region, where NW2 is pinched off, to evaluate the superconducting gap in contact with the device and its dependence on the magnetic field. Fig. 33(a) shows G against V_{sd}. We observed two large peaks attributed to quasiparticle tunneling, indicated by red arrows. These peaks correspond to $2\Delta/e$, where Δ is the superconducting gap; therefore, Δ is estimated as 185 μeV, which is a typical value of bulk Al. We also measured G as a function of V_{sd} and the magnetic field B in Fig. 33(b). The gap decreases by increasing B and finally disappears at $B = 160$ mT, which is the critical field of the junction. This is a typical result for the s-wave superconductor Al.

C.   Multiple Andreev reflection and conductance quantization outside the superconducting gap

Fig.34 shows typical results of G against V_{sd} in the plateau regions of (2,0),(0,2), and (2,2). Multiple structures are observed in $V_{sd} < 2\Delta/e \approx 370$ μeV in all regions. These peaks are due to MAR. Moreover, for a large bias voltage outside the superconducting gap, G converges at a constant conductance value of (m + n) $\times 2e^2/h$ for the (m,n) plateau [56, 57]. These results support the ballistic nature of the junction and the measured points in Fig. 34 are certainly on the normal state conductance plateaus of the DNW.
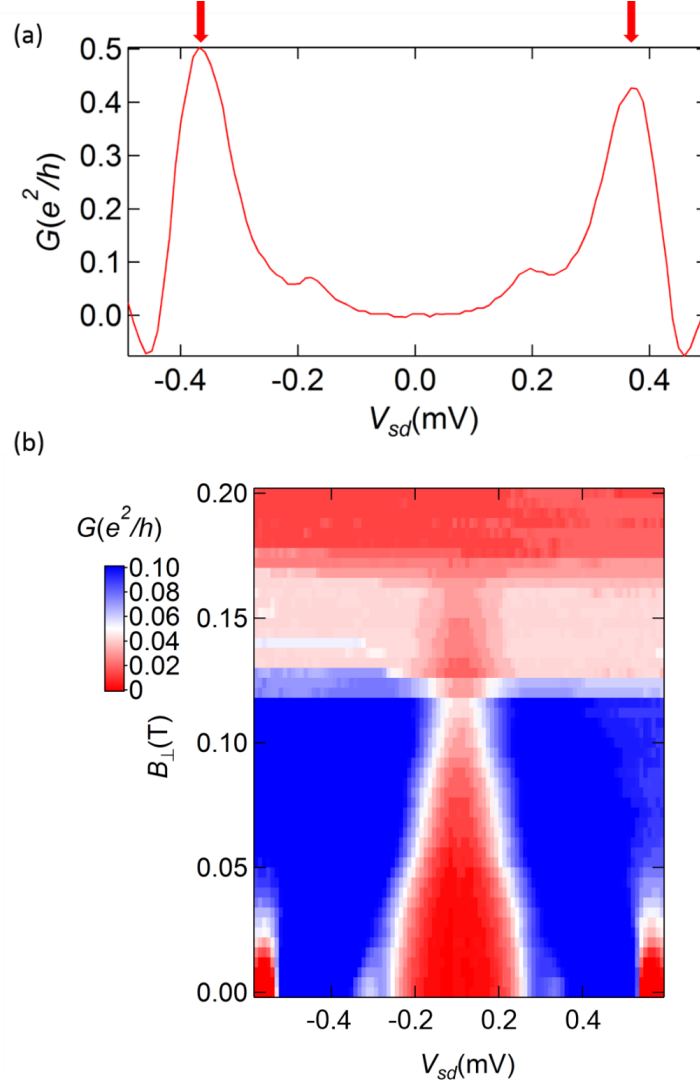
FIG. 33. Differential conductance G of the DNW device [1]. (a) G as a function of V_{sd} at $B = 0$ T. The two red peaks at $V_{sd} = \pm 370$ μeV indicate the magnitude of the superconducting gap due to quasiparticle tunneling at $|V_{sd}| = 2\Delta/e$. The estimated gap $\Delta = 185$ μeV is consistent with the superconducting gap of Al. The small peaks at $|V_{sd}| = \Delta/e$ are due to the AR. (b) G as a function of V_{sd} and B. The superconducting gap becomes smaller and closes completely at $B = 160$ mT.
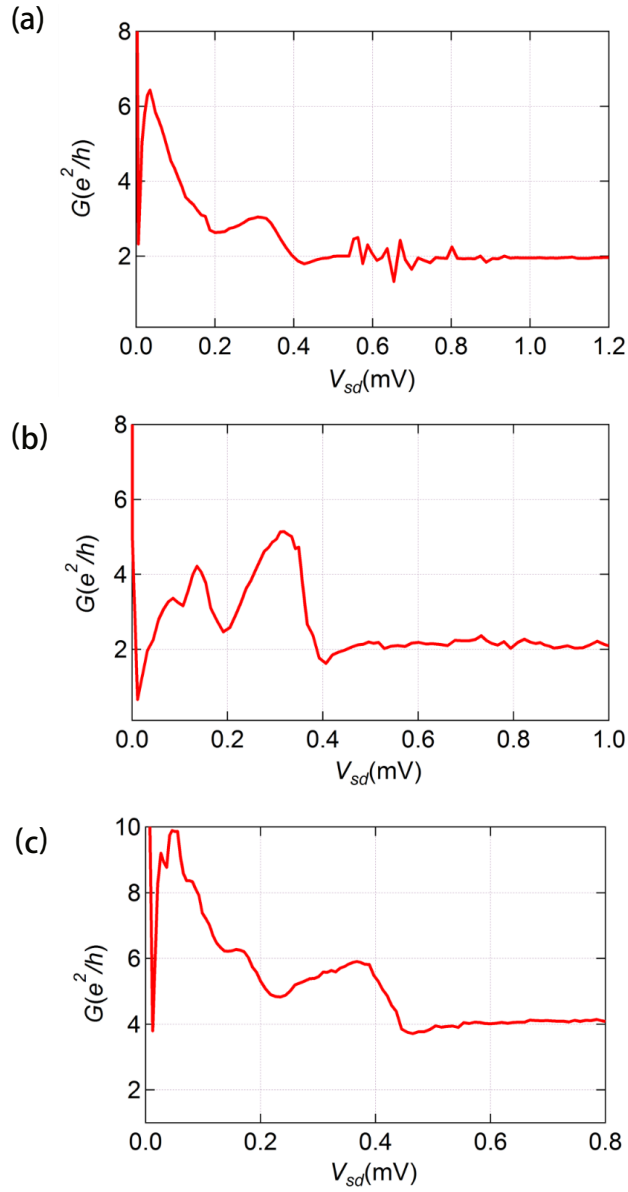
72

FIG. 34. G as a function of V_{sd} at $B = 0$ T for some points on the plateau of (m,n) in Fig. 32(a). Typical results for the plateau of (a) (2,0) at $V_{g1} = -8.75$ V and $V_{g2} = -5.58$ V, (b) (0,2) at $V_{g1} = -17.0$ V and $V_{g2} = -5.00$ V, and (c) (2,2) at $V_{g1} = -10.6$ V and $V_{g2} = 2.20$ V. The conductance outside the superconducting gap becomes $2e^2/h$ in (a), $2e^2/h$ in (b), and $4e^2/h$ in (c) [1].

D.   Measurement points for supercurrent

The flow of the supercurrent through the SNW and the DNW was studied by choosing several points in each (m,n) region, measuring the supercurrent, and deriving the mean value and standard deviation of $I_{sw}(m,n)$, which is the switching current in (m,n). The measured points, shown in Fig. 35, are represented by circles on the surface plot of G of Fig. 32. The blue, red, and purple points are in the SNW of NW1, SNW of NW2, and DNW regions. We note that all the points in each (m,n) region coincide with the value of $(m+n) \times e^2/h$ within the error of $\pm 0.1 \times 2e^2/h$.

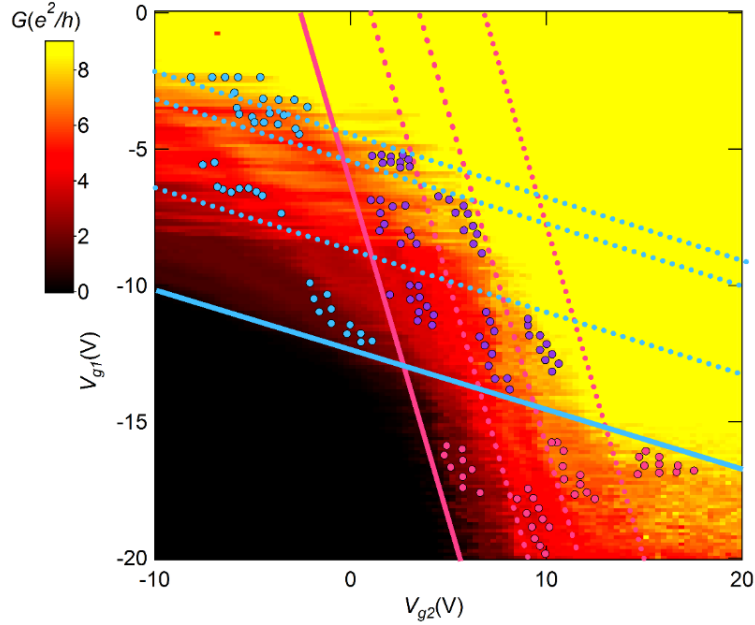FIG. 35. Points at which the supercurrent was measured at $B = 0$ T indicated on the surface plot of G as a function of V_{g1} and V_{g2} at $B = 250$ mT of Fig. 32. More than ten points were chosen for supercurrent measurement in each region [1].

E. Supercurrent in SNW

Next, we measured the differential resistance R against bias current I without applying a magnetic field to measure the supercurrent. Fig. 36(a) and (b) show typical results in the SNW region of NW1 and NW2. The resistance R becomes almost zero in the finite range of the bias current at approximately $I = 0$ A, which represents the supercurrent flowing through NW1 or NW2. We determined the peak positions of R as the magnitude of the supercurrent in each measurement. We chose several points on the same plateaus and took their average (see Fig. 35 about the points). Fig. 36(c) and (d) show the average switching current against G plots of NW1 and NW2, respectively.

F. Supercurrent in DNW

We measured the supercurrent in the DNW regions of (2,2), (4,2), (6,2), (2,4), (2,6), and (4,4) to study the CPS contribution depending on the number of 1D channels. Fig. 37(a) shows typical results in (2,2) (black), referring to (2,0) and (0,2) (blue and red, respectively). Similarly, Fig. 37(b) shows the results in (4,4) (black) with (4,0) and (0,4) (blue and red, respectively). In Fig. 37(a), the typical result $I_{sw}(2,2) = 11.3$ nA is much larger than the sum of $I_{sw}(2,0) + I_{sw}(0,2) = 4.78$ nA. Fig. 37(c) shows $I_{sw}(m,n)$ against $G(m,n)$ plotted by purple triangles in the DNW and $I_{sw}(m,0) + I_{sw}(0,n)$ against $G(m,0) + G(0,n)$ by pink circles in the SNW regions. Certainly, $I_{sw}(m,n)$ is larger than the sum of $I_{sw}(m,0)$ and $I_{sw}(0,n)$ for all values of m and n. The contribution of I_{sw} for the respective NWs is due to the contribution of the local pair tunneling (LPT) to the supercurrent. In the situation where both NWs contribute to the supercurrent, CPS is observed

as the difference between I_{sw} measured in DNW and the sum of I_{sw} measured for the respective NWs. Incidentally, because this device does not contain any QDs, the CPS mechanism cannot be explained by the electrostatic energy or Coulomb blockade effect of the dots, as previously reported.
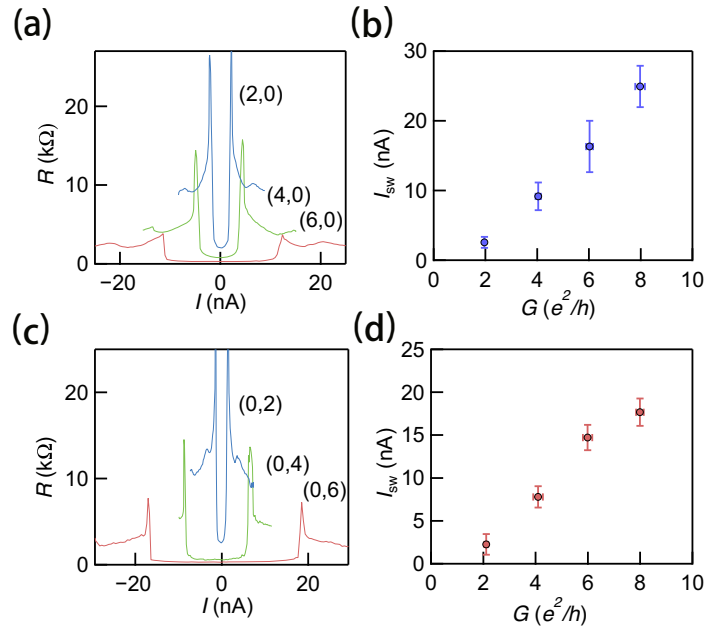

FIG. 36. Supercurrent in SNW regions [1]. (a) Typical R as a function of I at $B = 0$ T at several blue points in Fig. 35 on the conductance plateaus of (2,0), (4,0), and (6,0). The supercurrent flows through the Josephson junction in the range of $R \approx 0$ kΩ; I_{sw} is evaluated from the peak of R. (b) I_{sw} vs. G derived from the results in the SNW of the NW1 region of Fig. 35. The bars indicate variations in the measurements of I_{sw} and G at certain points in Fig. 35. (c) and (d) Identical plots to (a) and (b) in regions of (0,2),(0,4), and (0,6).
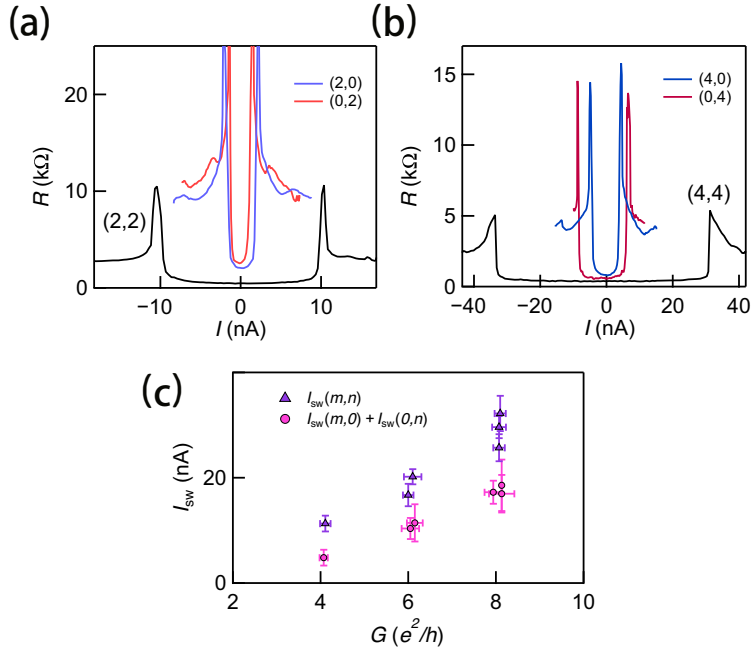
FIG. 37. Supercurrent in the DNW regions, and comparison with that in SNW regions [1]. (a) Typical R as a function of I at $B = 0$ T at several blue points in Fig. 35 on the conductance plateaus of (2,0), (0,2), and (2,2); I_{sw} in (2,2) is explicitly larger than the sum of $I_{sw}(2,0)$ and $I_{sw}(0,2)$. (b) R as a function of I on the conductance plateaus of (4,0), (0,4), and (4,4). Similar to (a), $I_{sw}(4,4)$ is much larger than the sum of $I_{sw}(4,0)$ and $I_{sw}(0,4)$. (c) $I_{sw}(m,n)$ vs. $G(m,n)$ in the conductance plateau regions (2,2), (2,4), (4,2), (2,6), (6,2), and (4,4), respectively. For comparison, the sum of $I_{sw}(m,0)$ and $I_{sw}(0,n)$ vs. the sum of $G(m,0)$ and $G(0,n)$ is plotted. The bars represent the variations in the measurements of I_{sw} and G at certain points on the respective plateaus. The difference between $I_{sw}(m,n)$ and the sum of $I_{sw}(m,0)$ and $I_{sw}(0,n)$ is the CPS contribution.

Other possible reasons for the enhancement of I_{sw}, such as macroscopic quan-

tum tunneling (MQT), thermal effects, and Joule heating also need to be considered. First, we consider the crossover temperature of MQT. We estimated the quality factor Q and plasma frequency ω using a junction capacitance of less than 100 fF and the junction resistance measured in Fig. 32, resulting in $Q = 0.1$ and $\omega = 10^{10}$ [28, 74]. Using this quality factor and theoretical representation of the crossover temperature in MQT $T_cr = \frac{\hbar\omega}{2\pi k_B}(1 + Q^2/4)^{1/2} - Q/2$ [75], we estimated $T_{cr} \approx 20$ mK, which is lower than the base temperature of 50 mK. Therefore, we can ignore the MQT in the junction. Second, we considered the crossover temperature between the thermal activation regime and tunnel regime using the RCSJ model. We found that the crossover temperature is also approximately 20 mK. Therefore, the junction is in the thermal activation regime, and we should consider the thermal effect. We analyzed the magnetic field dependence more precisely to determine whether the aforementioned thermal effect causes the enhancement of the measured I_{sw}. If the estimated I_{sw} is smeared owing to thermal noise [76], $I_{sw}(m, 0) + I_{sw}(0, n)$ is not proportional to the number of channels. Fig. 38(a) is $I_{sw}(m, 0) + I_{sw}(0, n)$ vs. $G(m, 0) + G(0, n)$ at $B = 80, 120$ mT, where the magnetic field suppresses the enhancement of I_{sw} at 0 T, and the thermal effect should have an important role in the estimation of I_{sw} because the obtained I_{sw} is lower than that at 0 T. We found that $I_{sw}(m, 0) + I_{sw}(0, n)$ measured at $B > 80$ mT follows the proportionality of $G(m, 0) + G(0, n)$, corresponding to the number of channels in the NWs. This supports the hypothesis that the smearing is independent of the enhancement of I_{sw} at approximately 0 T. We note that the differential resistance is measured by a lock-in technique with finite excitation. We converted the excitation we used into the current through the junction, resulting in 1 nA. Therefore, the finite resistance around zero bias current occurs owing to the finite excitation from the measurement and a possible offset of the lock-in-amplifier.

78

Joule heating can be evaluated as 200 mK using the thermal model [77]. The heating power in the DNW region is distributed to the two NWs and is weaker than in the SNW region. This may cause an enhancement. We measured the temperature dependence of $I_{sw}(2,2)$ in Fig. 38(b). If Joule heating is responsible for the enhancement, $I_{sw}(2,2)$ at 260 mK should be the same as that at 50 mK. However, the measured $I_{sw}(2,2)$ at 260 mK is 9 nA, which is still larger than $I_{sw}(2,0) + I_{sw}(0,2) = 5$ nA. If the enhancement is due to Joule heating, the heating should be 450 mK. This is not completely realistic. This conclusion enables us to rule out the contribution by Joule heating. We note that, because the junction is short ballistic, the heating may be overestimated.
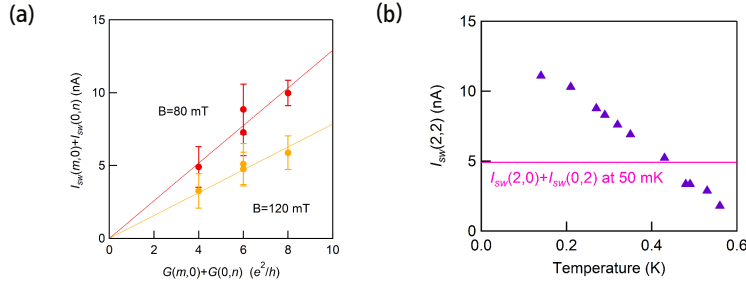

FIG. 38. (a) $I_{sw}(m,0) + I_{sw}(0,n)$ vs. $G(m,0) + G(0,n)$ measured at $B = 80$ mT (shown as red circles) and $B = 120$ mT (indicated by yellow circles) [1]. (b) $I_{sw}(2,2)$ as a function of temperature. $I_{sw}(2,2)$ below 460 mK is larger than $I_{sw}(m,0) + I_{sw}(0,n)$ at 50 mK, shown as a pink line [1].

G.   CPS efficiency

We evaluated the CPS efficiency η, defined by

$$\eta = \frac{I_{sw}(m,n) - (I_{sw}(m,0) + I_{sw}(0,n))}{I_{sw}(m,n)} \times 100 \ [\%]. \tag{56}$$

The estimated efficiency of $\eta(m,n)$ is shown in Fig. 39. The values in the (2,2), (4,2), (6,2), (2,4), (2,6), and (4,4) regions are 57.3, 31.6, 27.8, 48.8, 41.7, and 47.4 %, respectively. A value of η that is greater than 50 % means that the contribution to the supercurrent of CPS is dominant over that of LPT. We note that the two split electrons from the CPS components flow through the NWs as coherent single pairs, indicating that quasiparticle tunneling makes no substantial contribution. We consider the difference of the efficiency in each region. For example, $\eta(2,2)$ exceeds 50 % for (2,2). This indicates that the LPT component is suppressed. This can be explained by the theoretical model of CPS in the junction of a superconductor connected to two Tomonaga–Luttinger liquid (TLL) models [78, 79]. In this model, the TLL parameter $K_c = 1$, which means the absence of electron–electron interaction, indicates the probability of CPS and LPT is the same. This equates to the simple problem of which electron moves into which NW. On the other hand, when $K_c < 1$ in the case of electron–electron interaction, the LPT process is more difficult and less likely to occur than CPS. Therefore, $\eta(2,2) = 57.3$ % indicates that the presence of electron–electron interactions is important for understanding the mechanism of CPS in one dimension. We note that InAs wires have strong 1D electron–electron interactions because the small effective electron mass in the InAs wires induces a stronger spatial confinement [80].

η is asymmetric with each m and n. Although G in the normal state is the same in (4,2) and (2,4), $\eta(4,2)$ is smaller than $\eta(2,4)$. Similarly, $\eta(6,2)$ is smaller than $\eta(2,6)$. These features are assigned to the asymmetric carrier densities of the respective NWs in the proximity region. We see that NW1 is fully covered with Al; however, NW2 is not Al, thus the proximity region of NW1 has a higher carrier

$I_{sw}(8,0) =$ 24.9 ± 2.97 nA			
$I_{sw}(6,0) =$ 16.3 ± 3.69 nA	$I_{sw}(6,2) =$ 25.7 ± 2.58 nA **27.8%**		
$I_{sw}(4,0) =$ 9.16 ± 2.34 nA	$I_{sw}(4,2) =$ 16.7 ± 2.13 nA **31.6%**	$I_{sw}(4,4) =$ 32.2 ± 3.34 nA **47.4%**	
$I_{sw}(2,0) =$ 2.56 ± 0.78 nA	$I_{sw}(2,2) =$ 11.3 ± 1.49 nA **57.3%**	$I_{sw}(2,4) =$ 20.2 ± 1.45 nA **48.8%**	$I_{sw}(2,6) =$ 29.6 ± 2.10 nA **41.7%**
	$I_{sw}(0,2) =$ 2.26 ± 1.20 nA	$I_{sw}(0,4) =$ 7.79 ± 1.23 nA	$I_{sw}(0,6) =$ 14.7 ± 1.47 nA, $I_{sw}(0,8) =$ 17.6 ± 1.59 nA

FIG. 39. Schematic table of I_{sw}, which includes the averages and variations, and CPS efficiency η, for various values of m and n; I_{sw} is enhanced owing to the CPS for all conductance plateaus. The efficiency η is greater than 50 % in (2,2) [1].

density than that of NW2. We confirm this from the pinch-off values of each NW; the NW1 pinch-off voltage at $V_{g2} = 0$ V is $V_{g1} \approx -12$ V, whereas for NW2 at $V_{g1} = 0$ V, it is $V_{g2} \approx -2$ V. In theory, the lower carrier density in the NWs results in a small value of K_c in the TLL, which means stronger electron–electron interaction than kinetic energy; thus, the expected η becomes larger. Therefore, the stronger electron–electron interaction of NW2 than NW1 has the effect of a more significant suppression of LPT than in NW1. This could be the reason for the asymmetric efficiency of $\eta(4, 2) < \eta(2, 4)$ and $\eta(6, 2) < \eta(2, 6)$.

Furthermore, we found that η decreases as the number of NW conduction channels increases. This is also due to the weaker electron–electron interaction at higher carrier densities of the respective NWs. Therefore, smaller values of η are obtained with more channels.

H. Gap energy estimation

We discuss the case in which the energy of CPS or LPT contributes to the superconducting gap energy. We define the ratio of the induced superconducting gap energy due to CPS or LPT as follows:

$$\xi(m,n) = \frac{\Delta_{CPS}(m,n)}{\sqrt{\Delta_{NW1}(m,0)\Delta_{NW2}(0,n)}}, \tag{57}$$

where $\Delta_{CPS}(m,n)$, $\Delta_{NW1}(m,0)$, and $\Delta_{NW2}(0,n)$ are the superconducting gap energies of the interwire superconductivity via CPS, the intra-wire superconducting gap energy via the LPT of NW1, and that of NW2, respectively. Thus, ξ becomes a measure for determining whether the DNW is nontrivial or trivial. When ξ is greater than one, it satisfies the condition for the realization of MFs or PFs in DNW without any magnetic field. The superconducting gap in the short ballistic Josephson junction with R_n is represented as $R_n I_{sw} = \pi\Delta/e$ [62, 81]. Therefore, the superconducting energy of $\Delta_{CPS}(m,n)$, $\Delta_{NW1}(m,0)$, $\Delta_{NW2}(0,n)$ are estimated as $G(m,n)^{-1}(I_{sw}(m,n) - (I_{sw}(m,0) + I_{sw}(0,n)))$, $G(m,0)^{-1}I_{sw}(m,0)$, and $G(0,n)^{-1}I_{sw}(0,n)$, respectively. The estimated gap energies are shown in Fig. 40, where $\Delta_{NW1}(m,0)$, and $\Delta_{NW2}(0,n)$ decrease with smaller m and n, respectively. This is consistent with the theory that the extent to which LPT is suppressed is greater for fewer channels because of the stronger electron–electron interaction. Consequently, ξ becomes larger for fewer channels. In particular, ξ in the (2,2) and (2,4) regions becomes more than unity, and satisfies the condition for hosting MFs or PFs in our DNW system.

FIG. 40. Schematic table of estimated superconducting gap energies, and the ratio of the interwire and intrawire superconducting gap energies ξ in the (m, n) regions; ξ in $(2, 2)$ and $(2, 4)$ are greater than unity [1].

I. Dependence of CPS on the magnetic field

Fig. 41(a) shows the magnetic field dependence of $I_{sw}(2, 2)$ and $I_{sw}(2, 0) + I_{sw}(0, 2)$; $I_{sw}(2, 2)$ gradually decreases by $B = 80$ mT, whereas $I_{sw}(2, 0) + I_{sw}(0, 2)$ is almost the same. These two values almost converge at $B = 80$ mT, and then decrease in the same way. Therefore, a CPS component exists in the range of $B = 0$ to 80 mT, as shown by the purple shaded area in Fig. 41(a). A similar feature with a (2,2) region can be observed in other regions.

The theory states that the critical field of a superconducting thin film whose thickness is less than the coherence length and penetration length is inversely proportional to the film thickness [82]. This is applicable to our device when a magnetic field is applied perpendicular to the direction of the wire. As a result, the critical field of CPS, at which the Cooper pairs split into two different NWs, becomes half as large as that of LPT with Cooper pairs on either of the NWs.

83

Therefore, the dependence on B supports the fact that the enhancement of I_{sw} in the DNW regions has its origins in CPS.
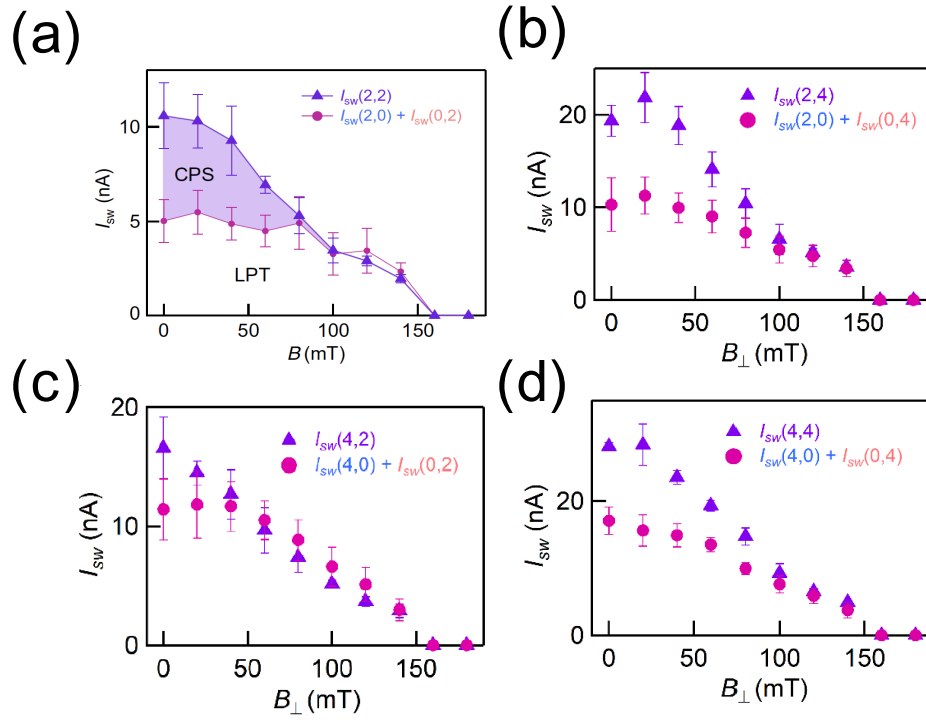

FIG. 41. Magnetic field dependence of CPS and LPT [1]. (a) $I_{sw}(2,2)$ and $I_{sw}(2,0) + I_{sw}(0,2)$ as functions of B. The CPS contribution vanishes at $B = 80$ mT. (b) $I_{sw}(2,4)$ and $I_{sw}(2,0) + I_{sw}(0,4)$ as a function of B. (c) $I_{sw}(4,2)$ and $I_{sw}(4,0) + I_{sw}(0,2)$ as functions of B. (d) $I_{sw}(4,4)$ and $I_{sw}(4,0) + I_{sw}(0,4)$ as a function of B.

J. Conclusion

In this study, we conducted supercurrent measurements on a ballistic DNW Josephson junction device to investigate CPS and LPT. We observed large CPS efficiency owing to the suppression of LPT by electron–electron interaction in the 1D NWs. In particular, we achieved a CPS efficiency of more than 50% by gate manipulation of the 1D electron interaction. In addition, we found that the CPS energy was dominant over the LPT energy when the number of the 1D channels was reduced to just one or two. Indicating that the necessary conditions for hosting MFs in the absence of a magnetic field can be satisfied in our CPS devices. This result clarifies the physics of CPS in one dimension and paves the way for the engineering of MFs using CPS.

Chapter 6

Half-integer Shapiro steps in a short ballistic InAs nanowire Josephson junction

I.   General introduction

In an SNS Josephson junction, a periodicity of 2π is usually present in the ABSs. When the superconductor becomes a topological superconductor, the periodicity changes to 4π because MFs exist at the edge of the topological superconductor. In such a case, odd-integer multiples of Shapiro steps are absent, such that we can see a trace of MFs in the Shapiro step measurement [8, 9, 83, 84]. In the preceding section, we demonstrated CPS in a ballistic Josephson junction and showed the possibility of realizing MFs in DNW architecture. As a next step, we have to understand the physics of the ballistic Josephson junction before undertaking research of MFs in a ballistic Josephson junction by measuring the Shapiro steps. When CPR is sinusoidal with a periodicity of 2π, it produces only the integer steps at $V = \pm nhf/2e(n = 1, 2, 3, \dots)$ in an overdamped Josephson junction [85, 86]. On the other hand, a ballistic semiconductor Josephson junction has a skewed CPR, which is expected to produce fractional steps. However, this has not yet been experimentally observed. To observe MFs in ballistic Josephson junctions using the Shapiro step measurement, it is first necessary to experimentally feature fractionalized Shapiro steps in ballistic Josephson junctions, and to

understand their physics. Here, we report the observation of the half-integer Shapiro step using the device shown in Fig. 29 originating from skewed sinusoidal CPR [2].

II. Measurement results

A. Fundamental device properties

We used the SNW device shown in Part IV and characterized the transport properties of the junction first under the normal state condition and then under the superconducting condition. Fig. 42(a) shows the differential conductance G as a function of the top gate V_g for temperature $T = 4$ K, which is greater than the critical temperature of Al. The pinch-off voltage at which the carrier density of the NW is depleted is $V_g = -12$ V. We completely controlled the carrier density of the NW of the junction to depletion. We also investigated G against a bias voltage V at $V_g = 0$ V and $T = 50$ mK in Fig. 42(b). We observed peaks at $V = \pm 2\Delta/ne(n = 1, 2, 3, \dots)$ due to MAR. Based on the conductance peaks of MAR, the superconducting gap Δ of Al is estimated to exist at 140 μV. In this measurement, the conductance peaks of MAR appear at these voltages for $n = 1, 2, 3$. This means that an elastic AR occurs at both interfaces of the Al contact and the NW. Therefore, the interfaces are sufficiently clean such that our junction is ballistic at $V_g = 0$ V [87]. Fig. 42(c) shows the $I - V$ curves of our junction at $V_g = 0$ V and $T = 50$ mK. The red (blue) curve represents the downward (upward) current sweep. The switching current I_{sw} corresponding to the magnitude of the supercurrent was estimated to be 40 nA.
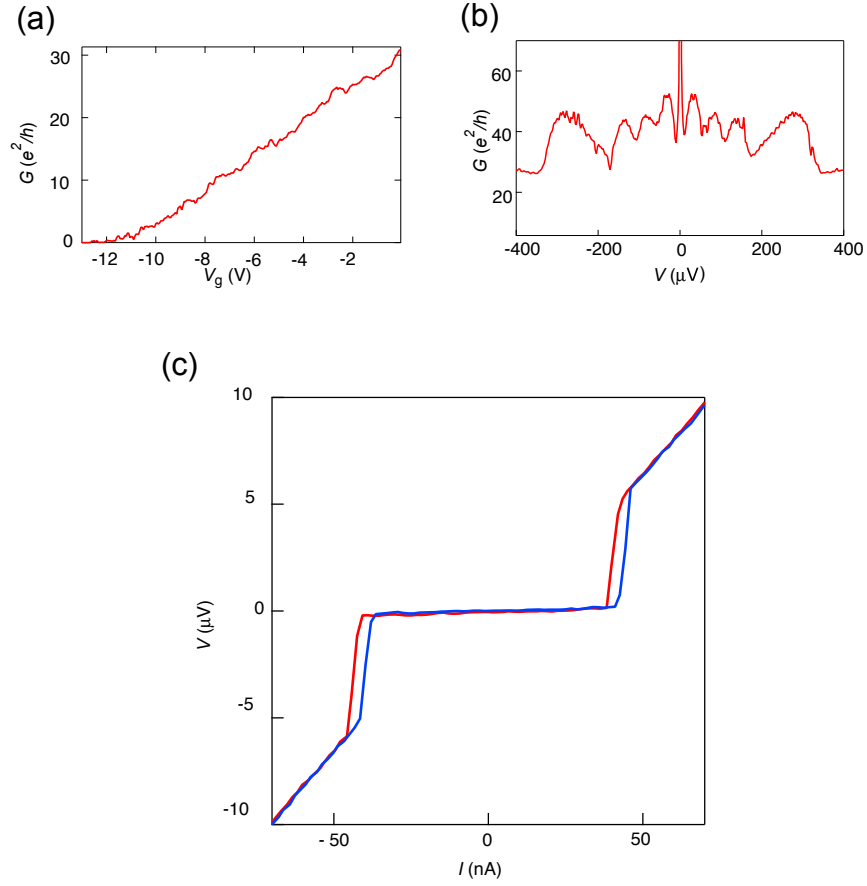
FIG. 42. (a) Conductance G as a function of V_g at $V = 1$ μV for $T = 4$ K. The device is pinched-off at $V_g = -12$ V [2]. (b) G against V at $V_g = 0$ V and $T = 50$ mK. The conductance peaks are attributed to MAR [2]. (c) $I - V$ curves of our junction at $V_g = 0$ V and $T = 50$ mK. The red (blue) line corresponds to a downward (upward) current sweep [2].

B. Observation of half-integer Shapiro steps

We studied the AC Josephson effects or Shapiro steps by irradiating the SNW Josephson device. The measurements of the Shapiro steps were conducted at an applied frequency of $f = 4.2$ GHz. The black curve in Fig. 43(a) shows the $I - V$ curve at $f = 4.2$ GHz, $V_g = 0$ V, and the applied power $P = 6$ dBm. In addition to the conventional Shapiro steps observed at $V = nhf/2e(n = 1, 2, 3, \dots)$, additional steps are observed at half-integer multiples of hf/2e. In Fig. 44(a), we also observe half-integers at $P = 0$ dBm and $P = 15$ dBm. We note that the red curves in Fig. 43(a) and Fig. 44(a) are obtained from Fig. 44(b). The differential resistance R against I becomes zero at the integer steps shown by the red dotted line in Fig. 43(a). Half-integer steps are found in the trace of R vs. I as small dips between two sharp peaks.

Next, we consider the origin of the half-integer steps. The short ballistic CPR is expressed as in Eq. (27). The CPR is highly skewed from $\sin(\phi)$ of the conventional Josephson junction. Skewed CPR produces half-integer steps because CPR has higher harmonic components, which are fractions of 2π. We simulated the Shapiro steps from CPR with $\tau = 0.98$ and $T = 50$ mK. Fig. 43(b) shows the calculated result for $\beta = 0.008$, $f' = 0.095$, and $i_{\mathrm{ac}} = 2$ (see Eq. (29) for these parameters). The black solid (red dotted) line represents V (the differential resistance δR) against I/I_{sw}. It is obvious that the numerical calculation reproduces the experimentally observed half-integer steps. Furthermore, steps such as one-third or two-thirds of the steps, which reflect the higher components, can be obtained in our simulation. We expect to detect these steps if we prepare the experimental setup with higher resolution. We assumed that all the channels in the NW have the same τ in our calculation because it is difficult to determine τ
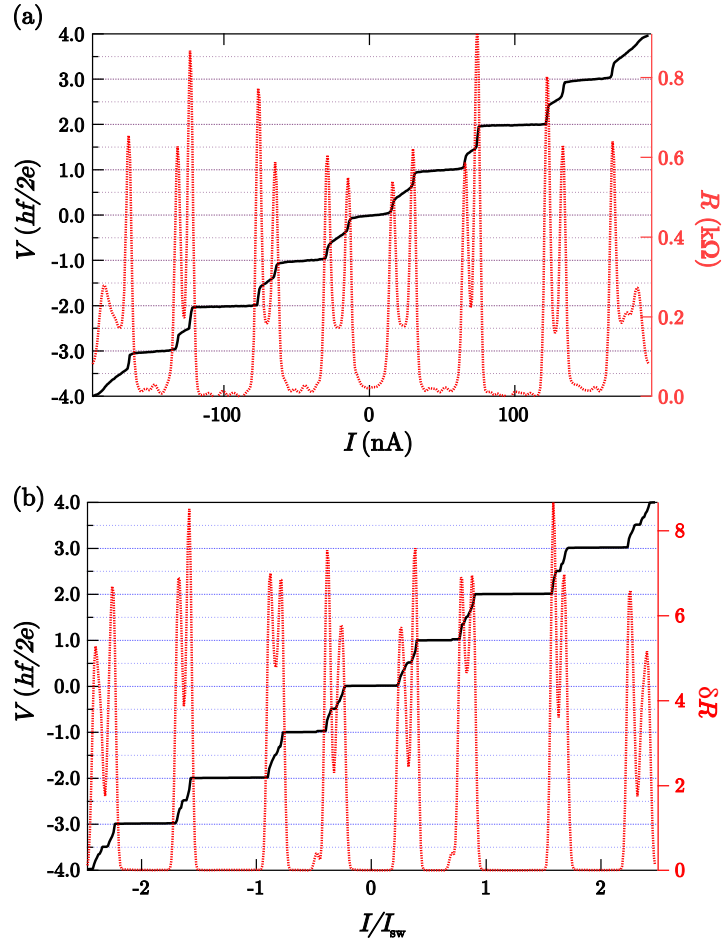
strictly for each channel.

FIG. 43. (a) Shapiro steps under microwave irradiation at $f = 4.2$ GHz, $V_g = 0$ V, and microwave power $P = 6$ dBm (black curve). The red curve is the resistance R of the $I - V$ curve [2]. (b) Numerical calculation of Shapiro measurement at $\beta = 0.008$, $f' = 0.095$, and $i_{ac} = 2$ (these parameters are explained in the text) [2].
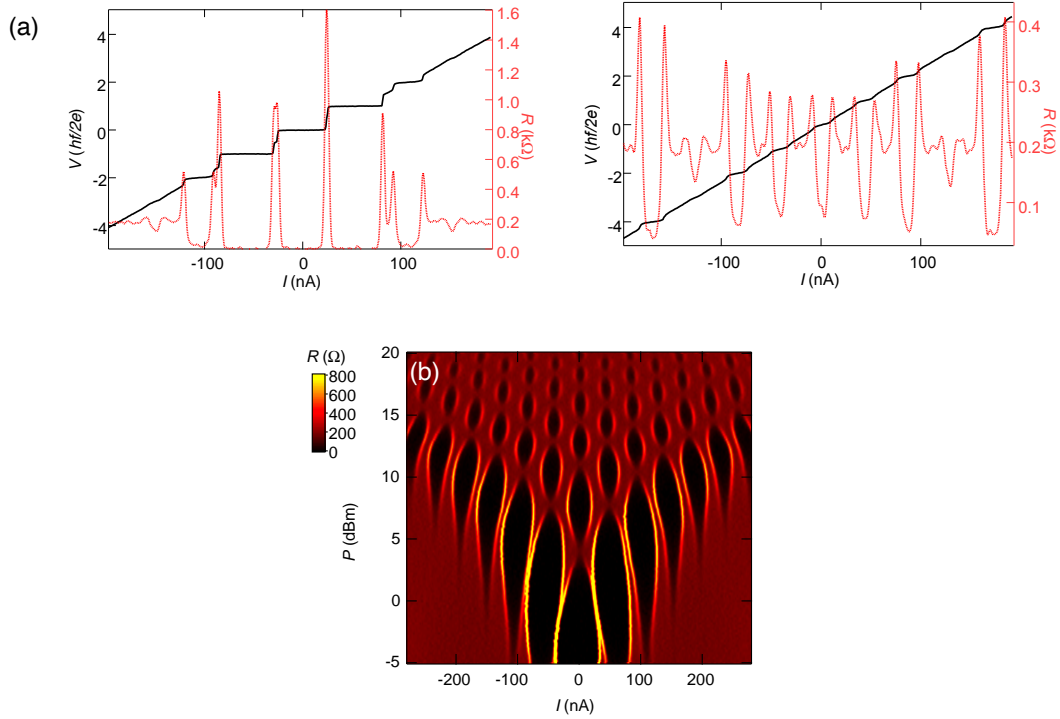
90

FIG. 44. (a) Shapiro steps (black curves) at $f = 4.2$ GHz, $V_g = 0$ V with $P = 0$ dBm (left panel) and $P = 15$ dBm (right panel). The red curves show R of the I–V curve [2]. (b) Color plot of R as a function of I and P at $f = 4.2$ GHz, $V_g = 0$ V, and $T = 50$ mK [2].

Additional half-integer steps were observed by conducting measurements by varying the microwave frequency and power. We show the measured results with $f = 3.7$ GHz and $f = 1.8$ GHz. The curves of Fig. 45(b) represent line profiles at $f = 3.7$ GHz from Fig. 45(a). The panels on the left and right represent the case of $P = 10$ dBm and $P = 15$ dBm. Fig. 45(c) shows the Shapiro steps measurements at $f = 1.8$ GHz. The curves in Fig. 45(d) represent the line profiles of $P = -16$ dBm (left panel) and $P = -10$ dBm (right panel).
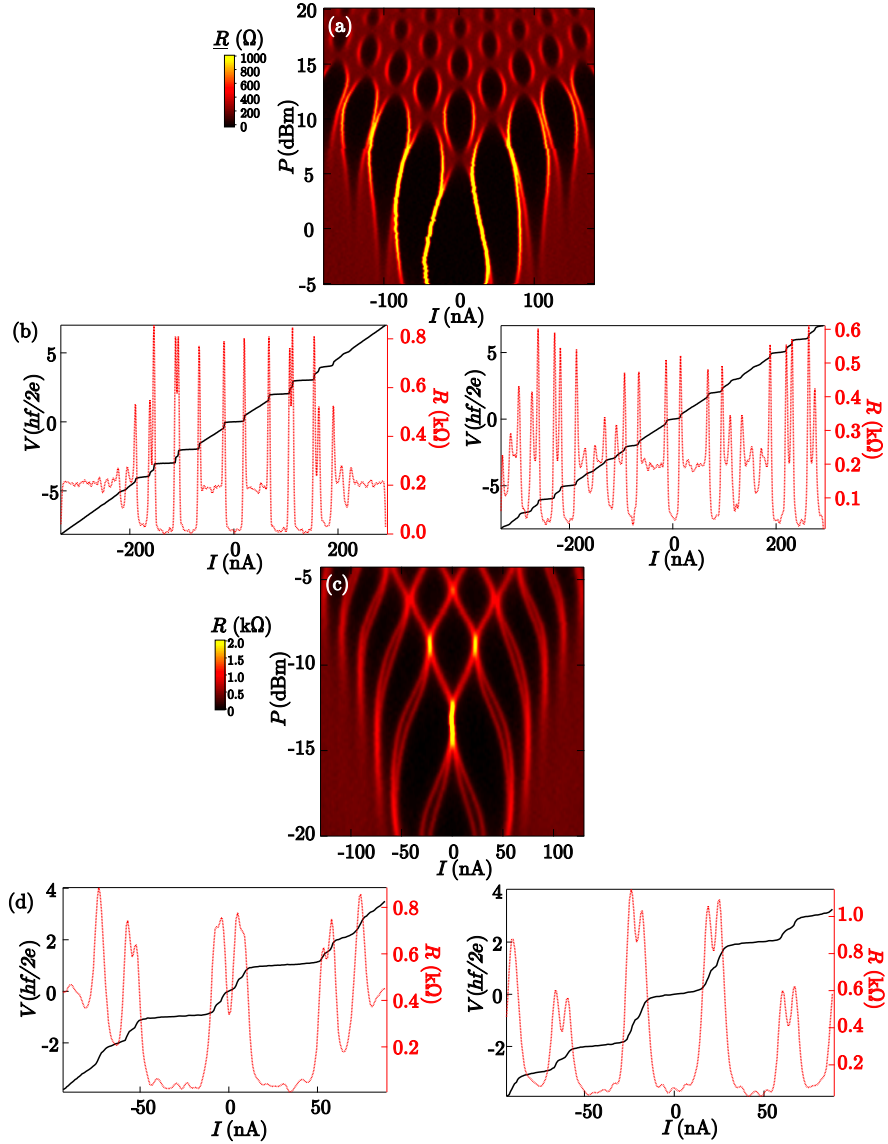
FIG. 45. Shapiro steps at other frequencies [2]: (a) Color plot of R as a function of I and P at $f = 3.7$ GHz and $V_{\mathrm{g}} = 0$ V. (b) Shapiro steps (black curves) at $f = 3.7$ GHz and $V_{\mathrm{g}} = 0$ V. Left panel: $P = 10$ dBm. Right panel: $P = 15$ dBm. The red curves show R of the I–V curve. (c) Color plot of R as a function of I and P at $f = 1.8$ GHz, $V_{\mathrm{g}} = 0$ V. (d) Shapiro steps (black curves) at $f = 1.8$ GHz, $V_{\mathrm{g}} = 0$ V. Left panel: $P = -16$ dBm. Right panel: $P = -10$ dBm. The red curves show R of the I–V curve.

C. Dependence of the half-integer steps on the gate voltage

The short ballistic CPR of Eq. (27) depends on both τ and T. To examine the relationship between the CPR skewness and the half-integer steps, we investigated I_{sw} vs. T at several V_g. Fig. 46(a) shows the dependence of I_{sw} at $V_{\mathrm{g}} = 0, -1, -2, -3$ V on T. The solid lines are the numerical fitting of the experimental results indicated by dots with the maximum of Eq. (27) with τ and the effective channel number as free fitting parameters. The experimental results are in good agreement with the simulated data using short ballistic CPR. Each τ at $V_g = 0, -1, -2$, and -3 V is estimated to be 0.98, 0.85, 0.89, and 0.7, respectively, from the numerical fitting. The term τ decreases with decreasing conductance by applying negative gate voltage. As shown in Fig. 46(b), the CPR is most highly skewed at $V_g = 0$ V among these voltages because τ at $V_g = 0$ V is almost unity.
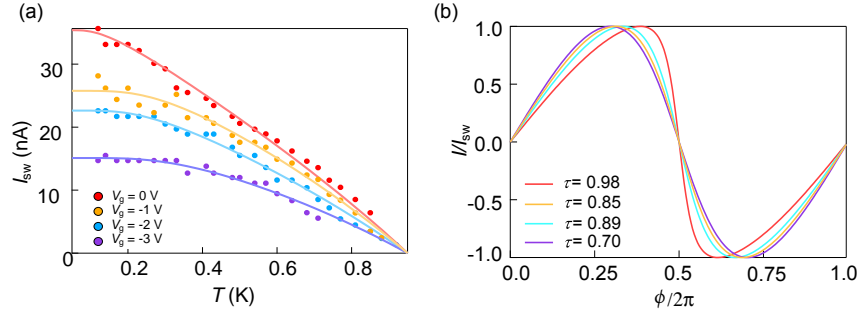

FIG. 46. (a) I_{sw} as a function of T for various values of V_g. The red, orange, blue, and purple dots correspond to $V_{\mathrm{g}} = 0, -1, -2, -3$ V, respectively, [2]. (b) Short ballistic CPR curves for $\tau = 0.98$ (red), $\tau = 0.85$ (orange), $\tau = 0.89$ (blue), and $\tau = 0.7$ (purple) at $T = 50$ mK [2].

We measured the dependence of the Shapiro steps on V_g at $f = 1.8$ GHz, $P =$

−17 dBm, and $T = 50$ mK (Fig. 46(a)). The half-integer steps disappear with decreasing V_g. We studied the relationship between β and τ because β is critical for understanding the junction dynamics. Fig. 47(b) shows the dependence of both β and τ on V_g; β is approximately 0.01 in the V_g range from 0 V to −3 V, indicating that the RCSJ circuit of our junction is overdamped. In contrast, τ decreases with decreasing V_g. Therefore, the V_g dependence of the half-integer steps is not attributable to β. We conclude that the disappearance of the half-integer steps with decreasing V_g is mainly due to the skewness of the CPR.
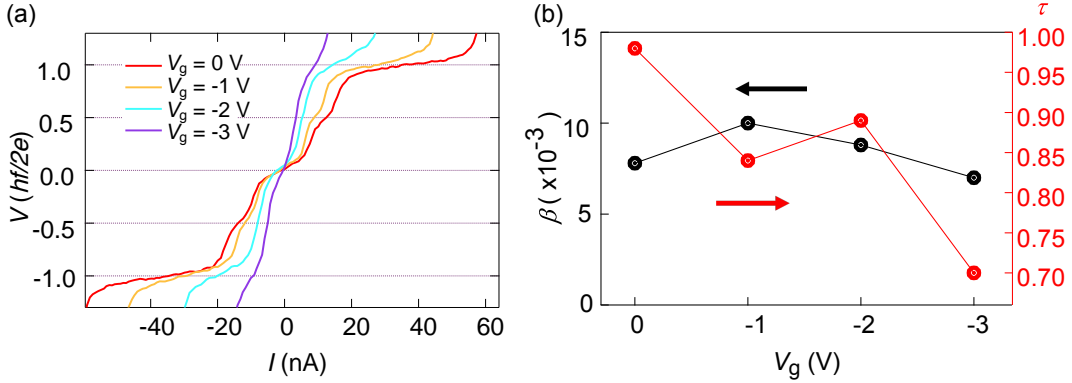

FIG. 47. (a) I–V curves at $V_g = 0, -1, -2$, and -3 V with $P = -17$ dBm and $f = 1.8$ GHz [2]. (b) β and τ as functions of V_g [2].

D. Temperature dependence of the half-integer steps

We measured the dependence of the Shapiro steps on T at $V_g = 0$ V. The simulated CPR with $\tau = 0.98$ at $T = 50, 150, 250$, and 750 mK is shown in Fig. 47(a), which shows that the CPR loses skewness as T increases. The $I - V$ curves measured under microwave irradiation between $T = 150 - 900$ mK are shown in

94

Fig. 47(b). The half-integer steps still appear, whereas the conventional Shapiro steps disappear as T increases. This is consistent with the experimentally observed dependence of the CPR on T in Fig. 47(a). This supports the assertion that the half-integer steps are attributed to the skewed CPR.
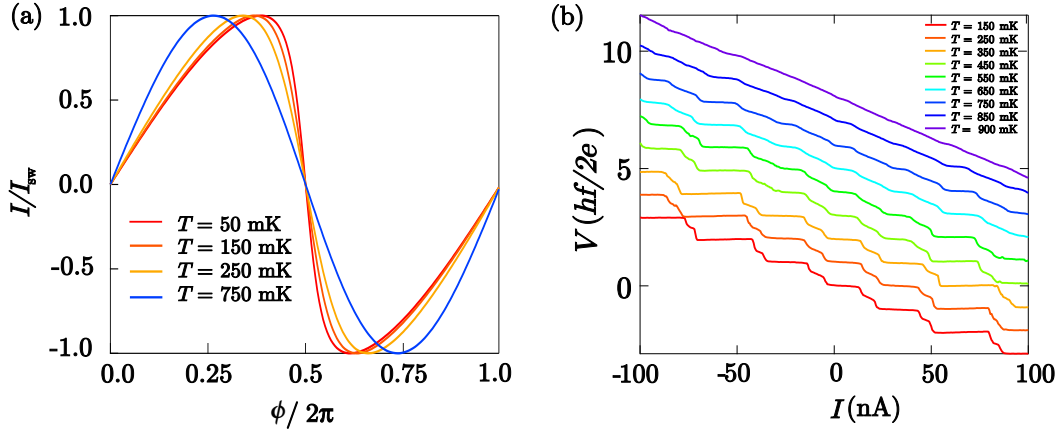

FIG. 48. (a) Short ballistic CPR curves for $T = 50$ mK (red), $T = 150$ mK (orange), $T = 250$ mK (yellow), and $T = 750$ mK (blue) at $\tau = 0.98$ [2]. (b) Dependence of the Shapiro steps on T at $f = 4.2$ GHz and $P = 11$ dBm. Each data line is offset by $hf/2e$, except for the data line for 150 mK [2].

E.   Temperature dependence of the integer steps

Finally, we show the normalized integer Shapiro steps as a ratio of the length of the integer steps at each T to that at $T = 150$ mk, which supports the assertion described above. Fig. 48 shows the normalized step length vs. T. Fig. 48(a),(b), and (c) corresponds to the steps with $n = 0, 1$, and 2, respectively. The circular points represent the experimental data at $V_g = 0$ V. The square and triangular

points indicate the numerical results using the RCSJ circuit with short ballistic CPR and sinusoidal CPR, respectively. The parameters used were $\tau = 0.98$ and $\beta = 0.008$. The experimental results coincide with the squares of the short ballistic Josephson junction rather than the triangles of the sinusoidal CPR. This also supports the assertion that our device is well characterized by the CPR of a short ballistic Josephson junction.
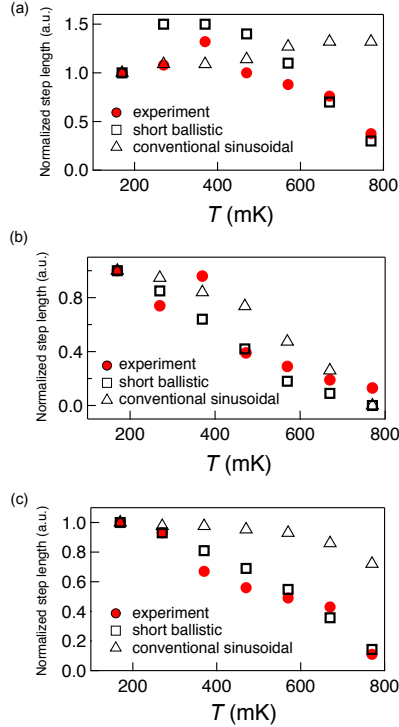

FIG. 49. T dependence of normalized step length ratio at $V = nhf/2e$ for (a) $n = 0$, (b) $n = 1$, and (c) $n = 2$. The circles, squares, and triangles correspond to the experimental results, the numerical simulation of the short ballistic CPR, and the numerical simulation of sinusoidal CPR, respectively, [2].

96

F.   Discussion

When the microwave frequency is greater than the energy relaxation and the energy gap in the SNS junction, the quasi-particles are directly excited across the gap by the microwave absorption, resulting in varying CPR. Therefore, this effect, known as the nonadiabatic effect, causes half-integer Shapiro [40–42]. The energy gap in the ballistic case corresponds to $I_{sw}R$. $I_{sw}R$ with our case of $f = 1.8$ GHz and $V_g = 0$ V is estimated as 33 μeV, which is much larger than $f = 1.8$ GHz. Furthermore, $I_{Sw}R$ is smaller with negative V_g. If the nonadiabatic effect is dominant, then the half-integer steps with smaller V_g of Fig. 47(a) should be observed clearly because the energy of $I_{Sw}R$ closely approaches that of f.

G.   Conclusion

We observed the half-integer Shapiro steps in the short ballistic Josephson junction of an InAs NW. We studied the origin of the experimentally observed half-integer steps by numerical calculations. A comparison of the V_g dependence of τ and the T dependence of I_{sw} between the numerical and experimental results enabled us to confirm the assertion that the half-integer steps originate from CPR skewness of short ballistic junctions. In addition, this result paves the way for the observation of MFs using the Shapiro response via the ballistic Josephson junction.

Chapter 7

Summary and Outlook

In this thesis, we explored the superconducting properties of InAs DNW or SNW Josephson junctions, with the goal of generating and detecting robust MBSs with no magnetic field. The major achievements are described in Chapter 4 to 6. In Chapter 4, we developed a fabrication method for ballistic Josephson junction samples using InAs NWs. Compared with previous fabrication techniques in our group, we achieved the following improvements:

- We refined the fabrication technique to improve the quality of electrical contacts between a SC and a NW.

- The distance between the SCs is considerably shortened to obtain a ballistic junction.

- The electron density of the NW is easily controlled using top gates above the NW.

In Chapter 5, we demonstrated CPS in 1D channels of a DNW for the first time:

- We succeeded in the fabrication of a ballistic SC-DNW-SC Josephson junction sample.

- The CPS efficiency was controlled with gate voltage and increased to dominate the supercurrent by increasing the 1D electron-electron interaction.

- The condition of inter-wire pairing strength ¿ intra-wire pairing strength $(\Delta_{CPS}^2 > \Delta_{NW1}\Delta_{NW2})$ necessary for the emergence of MBSs with no magnetic field.

In Chapter 6, we performed Shapiro step measurement with a ballistic InAs NW Josephson junction device for the first time and confirmed the specific properties of the ballistic junction.

- We fabricated a ballistic SC-InAs NW-SC Josephson junction sample.

- Half-integer Shapiro steps, which are consistent with calculations using CPR for the short ballistic junction, were observed, and their dependencies on temperature and gate voltage were well understood.

- The relationship between the short ballistic CPR and AC Josephson dynamics were clarified.

- We confirmed that the Shapiro step measurement could pave the way for observing MFs with no magnetic field.

Throughout the thesis, we demonstrated CPS in 1D channels of a SC-DNW-SC junction and revealed a necessary condition for generating MBSs in the absence of a magnetic field. We characterized and numerically analyzed the Shapiro-step features in the ballistic NW Josephson junction. We have deepened our knowledge of the physics of ballistic junctions and are now prepared to detect MBSs with the DNW system. Finally, we provide some notes on how to observe MFs.

- There is room for improvement of the SC-NW interface. In the real world, epitaxial deposition and other methods are being used to improve the interface quality.

- In particular, tuning the Fermi energy in the proximity region is important, if yet difficult. It is necessary to devise a gate electrode with pinpoint accuracy, avoiding the SC screening, to generate and detect MBSs.

- The mechanism of CPS generation in 1D channels is still not clear. It is important to at least evaluate the inter-wire and intra-wire pairing strengths correctly.

- To generate the MBSs at zero or weak magnetic fields, it is necessary to adjust the chemical potential of the proximity region at the cross points of the SOI split bands, as well as the asymmetry of the SOI energy between the NWs. For both, it is crucial to control the gate tuning of the two NWs, which remains challenging. There needs to be a technical development to devise gate electrodes on the two NWs with pinpoint accuracy to avoid SC screening.

- In reality, finite contributions of quasiparticles other than MFs are thought to be present in hybrid SC-NW junction devices. This will affect the error-free nature of topological quantum calculations, which is one of the greatest advantages of topological quantum calculations. Therefore, it is essential to resolve this issue.

Acknowledgement

The results in this paper could not be accomplished alone and are due to the help of many people.

I would like to express my gratitude to Professor Yasunobu Nakamura of the Graduate School of Department of Applied Physics, University of Tokyo. I belonged to a laboratory and was allowed to research freely.

for their support. Thank you.

[1] K. Ueda, S. Matsuo, H. Kamata, S. Baba, Y. Sato, Y. Takeshige, K. Li, S. Jeppesen, L. Samuelson, H. Xu, *et al.*, Science advances **5**, eaaw2194 (2019).

[2] K. Ueda, S. Matsuo, H. Kamata, Y. Sato, Y. Takeshige, K. Li, L. Samuelson, H. Xu, and S. Tarucha, Physical Review Research **2**, 033435 (2020).

[3] V. Mourik, K. Zuo, S. M. Frolov, S. Plissard, E. P. Bakkers, and L. P. Kouwenhoven, Science **336**, 1003 (2012).

[4] A. Das, Y. Ronen, Y. Most, Y. Oreg, M. Heiblum, and H. Shtrikman, Nature Physics **8**, 887 (2012).

[5] M. Deng, C. Yu, G. Huang, M. Larsson, P. Caroff, and H. Xu, Nano letters **12**, 6414 (2012).

[6] S. Nadj-Perge, I. K. Drozdov, J. Li, H. Chen, S. Jeon, J. Seo, A. H. MacDonald, B. A. Bernevig, and A. Yazdani, Science **346**, 602 (2014).

[7] Q. Liu, C. Chen, T. Zhang, R. Peng, Y.-J. Yan, X. Lou, Y.-L. Huang, J.-P. Tian, X.-L. Dong, G.-W. Wang, *et al.*, Physical Review X **8**, 041056 (2018).

[8] L. P. Rokhinson, X. Liu, and J. K. Furdyna, Nature Physics **8**, 795 (2012).

[9] J. Wiedenmann, E. Bocquillon, R. S. Deacon, S. Hartinger, O. Herrmann, T. M. Klapwijk, L. Maier, C. Ames, C. Brüne, C. Gould, *et al.*, Nature communications **7**, 1 (2016).

[10] S. D. Sarma, M. Freedman, and C. Nayak, Physics Today **59**, 32 (2006).

[11] S. D. Sarma, M. Freedman, and C. Nayak, npj Quantum Information **1**, 1 (2015).

[12] P. Recher and D. Loss, Physical Review B **65**, 165327 (2002).

[13] A. Andreev, Sov. Phys. JETP **20**, 1490 (1965).

[14] G. Blonder, m. M. Tinkham, and k. T. Klapwijk, Physical Review B **25**, 4515 (1982).

[15] P. Recher, E. V. Sukhorukov, and D. Loss, Physical Review B **63**, 165314 (2001).

[16] G. B. Lesovik, T. Martin, and G. Blatter, The European Physical Journal B-Condensed Matter and Complex Systems **24**, 287 (2001).

[17] V. Bouchiat, N. Chtchelkatchev, D. Feinberg, G. Lesovik, T. Martin, and J. Torres, Nanotechnology **14**, 77 (2002).

[18] C. Bena, S. Vishveshwara, L. Balents, and M. P. Fisher, Physical Review Letters **89**, 037901 (2002).

[19] N. M. Chtchelkatchev, G. Blatter, G. B. Lesovik, and T. Martin, Physical Review B **66**, 161320 (2002).

[20] P. Burset, W. J. Herrera, and A. L. Yeyati, Physical Review B **84**, 115448 (2011).

[21] P. Recher and D. Loss, Physical review letters **91**, 267003 (2003).

[22] L. Hofstetter, S. Csonka, J. Nygård, and C. Schönenberger, Nature **461**, 960 (2009).

[23] L. Herrmann, F. Portier, P. Roche, A. L. Yeyati, T. Kontos, and C. Strunk, Physical review letters **104**, 026801 (2010).

[24] J. Schindele, A. Baumgartner, and C. Schönenberger, Physical review letters **109**, 157002 (2012).

[25] L. Hofstetter, S. Csonka, A. Baumgartner, G. Fülöp, S. d' Hollosy, J. Nygård, and C. Schönenberger, Physical review letters **107**, 136801 (2011).

[26] A. Das, Y. Ronen, M. Heiblum, D. Mahalu, A. V. Kretinin, and H. Shtrikman, Nature communications **3**, 1 (2012).

[27] S. Baba, C. Jünger, S. Matsuo, A. Baumgartner, Y. Sato, H. Kamata, K. Li, S. Jeppesen, L. Samuelson, H. Xu, *et al.*, New Journal of Physics **20**, 063021

(2018).

[28] R. S. Deacon, A. Oiwa, J. Sailer, S. Baba, Y. Kanai, K. Shibata, K. Hirakawa, and S. Tarucha, Nature communications **6**, 1 (2015).

[29] S. Baba, S. Matsuo, H. Kamata, R. Deacon, A. Oiwa, K. Li, S. Jeppesen, L. Samuelson, H. Xu, and S. Tarucha, Applied Physics Letters **111**, 233513 (2017).

[30] J. Xiang, A. Vidan, M. Tinkham, R. M. Westervelt, and C. M. Lieber, Nature nanotechnology **1**, 208 (2006).

[31] C. Beenakker, in *Transport Phenomena in Mesoscopic Systems* (Springer, 1992) pp. 235–253.

[32] I. Kulik and A. Omel'yanchuk, Sov. J. Low Temp. Phys.(Engl. Transl.);(United States) **4** (1978).

[33] W. Haberkorn, H. Knauer, and J. Richter, physica status solidi (a) **47**, K161 (1978).

[34] E. M. Spanton, M. Deng, S. Vaitiekėnas, P. Krogstrup, J. Nygård, C. M. Marcus, and K. A. Moler, Nature Physics **13**, 1177 (2017).

[35] W. Stewart, Applied Physics Letters **12**, 277 (1968).

[36] D. McCumber, Journal of Applied Physics **39**, 3113 (1968).

[37] S. Shapiro, Physical Review Letters **11**, 80 (1963).

[38] A. Y. Kitaev, Physics-Uspekhi **44**, 131 (2001).

[39] A. Valizadeh, M. Kolahchi, and J. Straley, Journal of Nonlinear Mathematical Physics **15**, 407 (2008).

[40] P. Dubos, H. Courtois, O. Buisson, and B. Pannetier, Physical review letters **87**, 206801 (2001).

[41] F. Chiodi, M. Ferrier, S. Guéron, J. Cuevas, G. Montambaux, F. Fortuna, A. Kasumov, and H. Bouchiat, Physical Review B **86**, 064510 (2012).

[42] J. Basset, M. Kuzmanović, P. Virtanen, T. T. Heikkilä, J. Estève, J. Gabelli, C. Strunk, and M. Aprili, Physical Review Research **1**, 032009 (2019).

[43] J. Alicea, Reports on progress in physics **75**, 076501 (2012).

[44] Y. Oreg, G. Refael, and F. Von Oppen, Physical review letters **105**, 177002 (2010).

[45] J. Klinovaja and D. Loss, Physical Review B **90**, 045118 (2014).

[46] M. Deng, C. Yu, G. Huang, M. Larsson, P. Caroff, and H. Xu, Scientific reports **4**, 7261 (2014).

[47] S. M. Albrecht, A. P. Higginbotham, M. Madsen, F. Kuemmeth, T. S. Jespersen, J. Nygård, P. Krogstrup, and C. Marcus, Nature **531**, 206 (2016).

[48] M. Leijnse and K. Flensberg, Semiconductor Science and Technology **27**, 124003 (2012).

[49] S. B. Bravyi and A. Y. Kitaev, Annals of Physics **298**, 210 (2002).

[50] C. Nayak, S. H. Simon, A. Stern, M. Freedman, and S. D. Sarma, Reviews of Modern Physics **80**, 1083 (2008).

[51] D. J. Clarke, J. Alicea, and K. Shtengel, Nature communications **4**, 1348 (2013).

[52] D. Rainis and D. Loss, Physical Review B **85**, 174533 (2012).

[53] J. Klinovaja and D. Loss, Physical Review B **86**, 085408 (2012).

[54] C. Schrade, M. Thakurathi, C. Reeg, S. Hoffman, J. Klinovaja, and D. Loss, Physical Review B **96**, 035306 (2017).

[55] C. Thelander, M. Björk, M. Larsson, A. Hansen, L. Wallenberg, and L. Samuelson, Solid State Communications **131**, 573 (2004).

[56] Y.-J. Doh, J. A. van Dam, A. L. Roest, E. P. Bakkers, L. P. Kouwenhoven, and S. De Franceschi, science **309**, 272 (2005).

[57] H. Nilsson, P. Samuelsson, P. Caroff, and H. Xu, Nano letters **12**, 228 (2012).

[58] S. Abay, D. Persson, H. Nilsson, H. Xu, M. Fogelstrom, V. Shumeiko, and P. Dels-

ing, Nano letters **13**, 3614 (2013).

[59] I. van Weperen, S. R. Plissard, E. P. Bakkers, S. M. Frolov, and L. P. Kouwenhoven, Nano letters **13**, 387 (2013).

[60] S. Chuang, Q. Gao, R. Kapadia, A. C. Ford, J. Guo, and A. Javey, Nano letters **13**, 555 (2013).

[61] J. Kammhuber, M. C. Cassidy, H. Zhang, O. Gul, F. Pei, M. W. de Moor, B. Nijholt, K. Watanabe, T. Taniguchi, D. Car, *et al.*, Nano letters **16**, 3482 (2016).

[62] C. Beenakker and H. Van Houten, Physical review letters **66**, 3056 (1991).

[63] T. Nishio, T. Kozakai, S. Amaha, M. Larsson, H. A. Nilsson, H. Xu, G. Zhang, K. Tateno, H. Takayanagi, and K. Ishibashi, Nanotechnology **22**, 445701 (2011).

[64] R. Frielinghaus, I. Batov, M. Weides, H. Kohlstedt, R. Calarco, and T. Schäpers, Applied physics letters **96**, 132504 (2010).

[65] C.-X. Liu, J. D. Sau, T. D. Stanescu, and S. D. Sarma, Physical Review B **96**, 075161 (2017).

[66] C.-X. Liu, J. D. Sau, and S. D. Sarma, Physical Review B **97**, 214502 (2018).

[67] E. Prada, P. San-Jose, M. W. de Moor, A. Geresdi, E. J. Lee, J. Klinovaja, D. Loss, J. Nygård, R. Aguado, and L. P. Kouwenhoven, Nature Reviews Physics **2**, 575 (2020).

[68] D. B. Suyatin, J. Sun, A. Fuhrer, D. Wallin, L. E. Fröberg, L. S. Karlsson, I. Maximov, L. R. Wallenberg, L. Samuelson, and H. Xu, Nano letters **8**, 1100 (2008).

[69] S. Abay, D. Persson, H. Nilsson, F. Wu, H. Xu, M. Fogelström, V. Shumeiko, and P. Delsing, Physical Review B **89**, 214508 (2014).

[70] H. Kamata, R. S. Deacon, S. Matsuo, K. Li, S. Jeppesen, L. Samuelson, H. Xu, K. Ishibashi, and S. Tarucha, Physical Review B **98**, 041302 (2018).

[71] J. Klinovaja and D. Loss, Physical review letters **112**, 246403 (2014).

[72] H. Ebisu, B. Lu, J. Klinovaja, and Y. Tanaka, Progress of Theoretical and Experimental Physics **2016** (2016).

[73] C. Reeg, C. Schrade, J. Klinovaja, and D. Loss, Physical Review B **96**, 161407 (2017).

[74] P. Jarillo-Herrero, J. A. Van Dam, and L. P. Kouwenhoven, Nature **439**, 953 (2006).

[75] H. Grabert and U. Weiss, Physical review letters **53**, 1787 (1984).

[76] V. Ambegaokar and B. Halperin, Physical Review Letters **22**, 1364 (1969).

[77] S. Roddaro, A. Pescaglini, D. Ercolani, L. Sorba, F. Giazotto, and F. Beltram, Nano Research **4**, 259 (2011).

[78] S.-I. Tomonaga and J. R. Oppenheimer, Physical Review **74**, 224 (1948).

[79] J. Luttinger, Journal of mathematical physics **4**, 1154 (1963).

[80] Y. Sato, S. Matsuo, C.-H. Hsu, P. Stano, K. Ueda, Y. Takeshige, H. Kamata, J. S. Lee, B. Shojaei, K. Wickramasinghe, *et al.*, Physical Review B **99**, 155304 (2019).

[81] A. Furusaki, H. Takayanagi, and M. Tsukada, Physical Review B **45**, 10563 (1992).

[82] F. Harper and M. Tinkham, Physical Review **172**, 441 (1968).

[83] E. Bocquillon, R. S. Deacon, J. Wiedenmann, P. Leubner, T. M. Klapwijk, C. Brüne, K. Ishibashi, H. Buhmann, and L. W. Molenkamp, Nature nanotechnology **12**, 137 (2017).

[84] C. Li, J. C. de Boer, B. de Ronde, S. V. Ramankutty, E. van Heumen, Y. Huang, A. de Visser, A. A. Golubov, M. S. Golden, and A. Brinkman, Nature materials **17**, 875 (2018).

[85] M. Renne and D. Polder, Revue de physique appliquée **9**, 25 (1974).

[86] J. Waldram and P. Wu, Journal of Low Temperature Physics **47**, 363 (1982).

[87] M. Hurd, S. Datta, and P. F. Bagwell, Physical Review B **54**, 6557 (1996).